

Data assimilation considerations for improved ocean predictability during the Gulf of Mexico Grand Lagrangian Deployment (GLAD)



Gregg A. Jacobs ^{a,*}, Brent P. Bartels ^b, Darek J. Bogucki ^c, Francisco J. Beron-Vera ^d, Shuyi S. Chen ^d, Emanuel F. Coelho ^{a,e}, Milan Curcic ^d, Annalisa Griffa ^{f,d}, Matthew Gough ^d, Brian K. Haus ^d, Angelique C. Haza ^d, Robert W. Helber ^a, Patrick J. Hogan ^a, Helga S. Huntley ^g, Mohamed Iskandarani ^d, Falko Judt ^d, A.D. Kirwan Jr. ^g, Nathan Laxague ^d, Arnoldo Valle-Levinson ^h, Bruce L. Lipphardt Jr. ^g, Arthur J. Mariano ^d, Hans E. Ngodock ^a, Guillaume Novelli ^d, M. Josefina Olascoaga ^d, Tamay M. Özgökmen ^d, Andrew C. Poje ⁱ, Ad J.H.M. Reniers ^d, Clark D. Rowley ^a, Edward H. Ryan ^d, Scott R. Smith ^a, Peter L. Spence ^b, Prasad G. Thoppil ^a, Mozheng Wei ^a

^a Naval Research Laboratory, Stennis Space Center, MS, 39529, United States

^b Vencore Services and Solutions, Inc., Stennis Space Center, MS 39529, United States

^c Department of Physical & Environmental Sciences, College of Science and Engineering, Texas A&M University, Corpus Christi, TX 78412, United States

^d Rosenstiel School of Marine & Atmospheric Science, University of Miami, Miami, FL 33149, United States

^e Department of Physics, University of New Orleans, New Orleans, LA 70148, United States

^f Consiglio Nazionale Ricerche, Istituto Scienze Marine, La Spezia 19032, Italy

^g School of Marine Science and Policy, University of Delaware, Newark, DE 19716, United States

^h Department of Civil and Coastal Engineering, University of Florida, Gainesville, FL 32611, United States

ⁱ Department of Mathematics, College of Staten Island, City University of New York, NY 10314, United States

ARTICLE INFO

Article history:

Received 21 January 2014

Received in revised form 1 August 2014

Accepted 7 September 2014

Available online 16 September 2014

Keywords:

Ocean
Assimilation
Modeling
Gulf of Mexico
Drifter
Covariance

ABSTRACT

Ocean prediction systems rely on an array of assumptions to optimize their data assimilation schemes. Many of these remain untested, especially at smaller scales, because sufficiently dense observations are very rare. A set of 295 drifters deployed in July 2012 in the north-eastern Gulf of Mexico provides a unique opportunity to test these systems down to scales previously unobtainable. In this study, background error covariance assumptions in the 3DVar assimilation process are perturbed to understand the effect on the solution relative to the withheld dense drifter data. Results show that the amplitude of the background error covariance is an important factor as expected, and a proposed new formulation provides added skill. In addition, the background error covariance time correlation is important to allow satellite observations to affect the results over a period longer than one daily assimilation cycle. The results show the new background error covariance formulations provide more accurate placement of frontal positions, directions of currents and velocity magnitudes. These conclusions have implications for the implementation of 3DVar systems as well as the analysis interval of 4DVar systems.

Published by Elsevier Ltd.

1. Introduction

Ocean prediction across the globe has made great advances in recent decades (Bell et al., 2009). Its success depends critically on the process of assimilation that continually corrects a prior forecast with recent observations, a process utilized in meteorology for decades (Kalnay, 2003). Recent observations, prior information (a background state, denoted as \mathbf{x}_b) and dynamical understanding are combined to construct an optimal state estimate as an initial

condition for the subsequent forecast period (Malanotte-Rizzoli, 1996). To do so, assumptions must be made about the relationship between the observations and amongst the background state variables and about the uncertainty in each. In particular, the error covariance of the background state, denoted as \mathbf{P}_b , is a key piece of information as Daley (1996) points out: "The most important element in the statistical interpolation algorithm is the background error covariance. To a large extent, the form of this matrix governs the resulting objective analysis". Specification of appropriate covariances is difficult as stated by Talagrand (2003) "Construction of these error estimates is the most challenging and scientifically important task." Without confidence in the formulation, the

* Corresponding author. Tel.: +1 (228) 688 4720; fax: +1 (228) 688 4759.

E-mail address: Gregg.jacobs@nrlssc.navy.mil (G.A. Jacobs).

prediction process becomes suspect as Bennett (2002) points out, “It is difficult to develop covariances. It follows that the resulting inverse estimate or analysis of the circulation also lack credibility.” Yet formulations of \mathbf{P}_b are rarely tested due to insufficient observations (Brasseur et al., 2005). That there is room for further improvement is suggested by isolated examples, such as the one detailed in Section 2.

The ocean is severely under-sampled in both space and time, hindering advances of many studies (Derber and Rosati, 1989). The satellite era revolutionized ocean science in that respect: Since 1992, the continual presence of satellite altimeters in particular provides a preponderance of information on ocean variability across the globe (Fu, 2010). However, the satellite altimeter constellation remains inadequate for providing synoptic observations even of just the two-dimensional mesoscale field at the ocean surface along with associated fronts and eddies. Le Traon and Dibarboure (2002) demonstrated in the Gulf of Mexico that the lack of observation results in substantial errors in estimating eddy frontal positions. The ability to draw clear conclusions from prior examinations of possible specifications for \mathbf{P}_b is limited by the lack of data (Lermusiaux, 2002). As \mathbf{x}_b is often provided by a prior model forecast, Gawarkiewicz et al. (2011) estimate \mathbf{P}_b by evaluating a prior forecast with subsequent observations made northeast of Taiwan, thus relying on a single sample to estimate a subset of \mathbf{P}_b . It is difficult to obtain a large enough number of independent forecast events to gain statistical confidence. Consequently, the fundamental question remains: To what degree are assimilation assumptions leading to errors in ocean state estimation?

Our purpose here is to systematically evaluate several key assumptions of the ocean data assimilation methodology by utilizing the rich drifter data set of the Grand Lagrangian Deployment (GLAD). The Consortium for Advanced Research on Transport of Hydrocarbon in the Environment (CARTHE) deployed 295 CODE-type drifters in the northeastern Gulf of Mexico on July 20–July 31, 2012 (Poje et al., 2014; Olascoaga et al., 2013; Coelho et al., 2014). The unprecedented data density achieved by this campaign makes the assessment possible by sustaining coverage at high spatial density over several mesoscale ocean features and over two months. The primary focus here is on the lower frequency mesoscale circulation in the deep water as this is the typical dynamical target of operational ocean assimilation systems. The assimilation systems are designed to constrain the mesoscale, and thus the higher frequency solutions have forecast skill that is a function of the external forcing and the dynamical representation.

We investigate independent perturbations of several aspects of the \mathbf{P}_b formulation, evaluating the resulting forecasts against the dense GLAD drifter observations, which are not assimilated. Perturbed features include the amplitude of the background error variance, horizontal correlation length scales, flow dependent variations in correlations and time decorrelation scales. While the system employed here is an implementation of 3DVar, the findings also impact parameter choices for 4DVar systems, which are becoming more popular (Cobas-Garcia et al., 2012; Janečković et al., 2013; Ngodock and Carrier, 2014). The detailed study presented here permits the assessment of the relative importance of each of the tested pieces of the specification of \mathbf{P}_b . It also provides guidance for appropriate parameter choices, in particular the decorrelation time scales.

After presenting an example to motivate the search for improved data assimilation in Section 2 and a synopsis of the GLAD experiment in Section 3, we provide details of the model setup and the experiments with perturbations on the assimilation background errors in Section 4. The results are examined in Section 5, with discussion in Section 6 and conclusions in Section 7.

2. Are our assumptions suspect?

An example from the GLAD planning phase illustrates the shortcomings of present assimilation. Daily oceanic condition forecasts are provided by numerical model systems based on the Hybrid Coordinate Ocean Model (HYCOM) and the Navy Coastal Ocean Model (NCOM), both using the same data through 3DVar assimilation within the Navy Coupled Ocean Data Assimilation (NCODA) system (Barron et al., 2006, 2007; Cummings et al., 2009; Martin et al., 2009; Rowley, 2010; Rowley et al., 2010; Metzger et al., 2010; Smith et al., 2011).

Satellite-observed chlorophyll provides an indication of Lagrangian material transport. Lagrangian Coherent Structures (LCS), which outline material transport patterns (Haller and Yuan, 2000; Haller and Beron-Vera, 2012), are computed from HYCOM and NCOM model surface currents and compared to the chlorophyll observations (Fig. 1). In Fig. 1a, the chlorophyll plume from the high productivity area around 29°N 88°W has spread to the southeast. At 26°N 86.5°W, the plume turns and extends northward, implying an intense cyclonic feature at roughly 27°N 86°W. The LCS computed from both models cut across the chlorophyll plume at 27.5°N 87°W, more than 100 km north of the observed plume turning. Although chlorophyll is not an ideal tracer, a misalignment of this magnitude indicates poor agreement between model currents and observed material transport. In particular, neither system captures the cyclonic turning at 26°N.

The two forecast systems based on HYCOM and NCOM share the same input data and data assimilation methodology. The sea surface height anomaly (SSHA) along altimeter ground tracks during this time (Fig. 2) indicates a cyclonic circulation at 27°N 86°W that is intruding into the Loop Current Eddy (LCE) to the southwest. An interpolation of this data constructed by AVISO (Pascual et al., 2006) is used to calculate geostrophic currents, and the LCS based on the geostrophic currents aligns with the chlorophyll imagery (Fig. 2).

Given the 3 km model resolution, a second order finite difference can reasonably represent first order derivative wavelengths of 24 km and larger, and it can represent nonlinear terms such as advection of momentum at 48 km and larger wavelengths. These are scales smaller than those resolved by the satellite data. The numerical models will produce realistic dynamical processes that are unconstrained and hence could exhibit substantial differences relative to observations. However, the mislocation relative to the chlorophyll in Fig. 1 is on the order of 100 km, the same discrepancy occurs in both dynamical systems and the feature is resolved in the satellite derived LCS in Fig. 2. The conclusion is that the altimeter data contain the essential mesoscale features but the data assimilation used to correct both models is faulty. Clear visible satellite images such as this are relatively rare. Evaluations are qualitative and provide only one snapshot. Thus it is difficult to conduct a considered evaluation of possible error sources with only this data. Fortunately, the drifter observations from GLAD prove to be quite valuable.

3. The GLAD experiment

The drifters are similar to the CODE drifter design (Davis, 1985; Ohlmann et al., 2001), which intends to measure the upper 1 m averaged currents. Table 1 summarizes the deployment locations, dates, number of drifters in the groups (LSS, S1, S2, T1, L1, L2) and initial ocean conditions. Fig. 3 shows the number of active drifters during the experiment. Initial group deployment positions are noted in Fig. 4. Initially, the reduction in the number of drifters is due to fishermen recovering some, and Hurricane Isaac inflicts damage on the observation system in late August. The slow degradation over time is

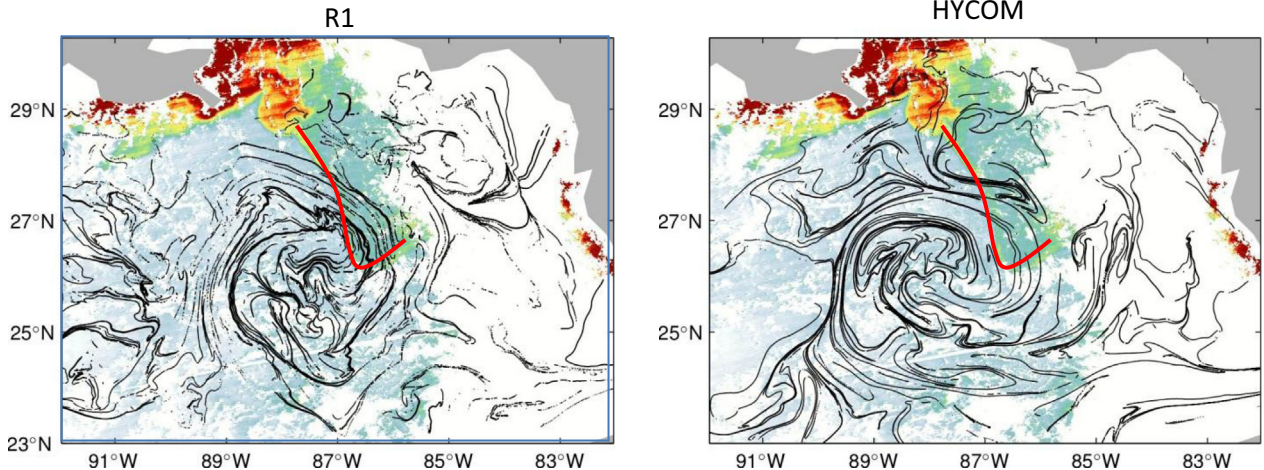


Fig. 1. Satellite-inferred chlorophyll from the MODIS Aqua sensor on July 12, 2012, in color. The red line qualitatively shows the core of the chlorophyll distribution. Superimposed are black lines of the Lagrangian Coherent Structures computed using the evolving model surface velocities from the NCOM R1 experiment (left) and HYCOM (right).

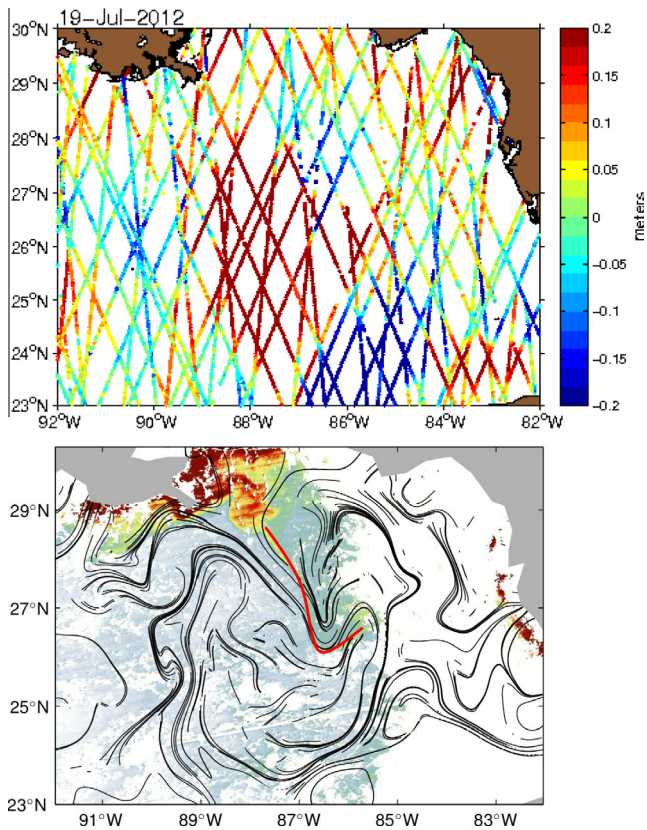


Fig. 2. The satellite SSHA from Jason-1, Jason-2 and CryoSat-2 (top) during the 35 days prior to July 19, 2012, indicate a cyclonic feature at 27°N 86°W. The July 12, 2012, satellite-inferred chlorophyll image from Fig. 1 with LCS computed from the geostrophic velocities of the AVISO composite of these data (bottom). The red line is the same as in Fig. 1, which is used to identify the chlorophyll core.

due to the limited battery life, and more than 100 units continued to report at the end of September 2012. Drifters report positions at 5-min intervals determined by GPS so that inferred velocities are quite accurate. Data gaps occur mostly due to adverse weather conditions, which require careful data processing to produce accurate trajectory and velocity estimates. Details on the drifter experiment and processing are provided in Olascoaga et al. (2013) and Coelho et al. (2014).

Fig. 4 schematically depicts the main circulation features which drifters encounter during August and September. As seen in Fig. 5, the drifter trajectories and model circulation indicate substantial mesoscale activity in this region of the Gulf. The main features are reproduced in the model. Typical discrepancies are misplacement of features such as August 22 where the cyclone at 87.5°W 27°N is observed further south than estimated by the model. Reproducing the shingle cyclones on the edge of the Loop Current Eddy is particularly difficult.

The drifter-inferred velocity spectral content is summarized by computing rotary spectra that contain the cyclonic (counterclockwise) and anticyclonic (clockwise) components (Fig. 6). The spectra are computed by averaging over all drifters the amplitude squared for each rotary component, and the amplitude spectrum is the square root of the averaged value. The spectra for both rotary components are dominated by low frequency motions due to the mesoscale circulation, both cyclonic and anticyclonic with greater energy in the cyclonic counterclockwise circulation. Also of significance is the clockwise energy surrounding one cycle per day (cpd) due to inertial oscillations. The inertial oscillations are a dominant feature in the observations driven by wind events, and thus are not stationary. Wind events generate inertial oscillations localized in time resulting in energy surrounding the inertial period spread over a wide band. A small peak near the M2 tidal frequency just under 2 cpd is also apparent. Both the inertial and semidiurnal bands contain high coherence between model and drifter spectra as will be shown later. The assimilation systems alter the energy at low frequencies during each analysis cycle. The variability below about 0.75 cpd is the focus of attention to understand how assumptions in the assimilation system affect predictability.

The remainder of this section provides a short description of the mesoscale features affecting the drifters over the two months. The experiments are compared relative to these features to understand with which features errors are associated. The Loop Current during July extends far northwest into the Gulf of Mexico, and the LCE detached just prior to the deployment, dominating the area south of the deployments. The LCE northern boundary is at about 27°N throughout the experiment. The eastern LCE boundary moves from 86°E to 88°E during August through September.

The general features are shown schematically in Fig. 4. The First Cyclone (FC) advects to the east along the periphery of the LCE, and by August 22, the FC begins to merge with the second cyclone (SC initially at 28°N 87°W). The SC advects the FC southward, substan-

Table 1

The summary of drifter deployment groups indicating the central location of the group, deployment date and number of drifters deployed.

Drifter group	Initial location	Deployment date (2012)	Number of drifters	Pertinent features and initial ocean conditions
LSS	DeSoto Canyon Area	July 20	20	Large scale survey covering the DeSoto Canyon
S1	28.8°N 88.1°W	July 22	90	Initially low southwestward flow
S2	29.2°N 87.6°W	July 26	90	Spanning observed Mississippi River fresh water front
T1	29.0°N 87.5°W	July 29	30	Head of DeSoto Canyon
L1, L2	27.8°N 89.2°W	July 30–31	60	Within first cyclone (FC)

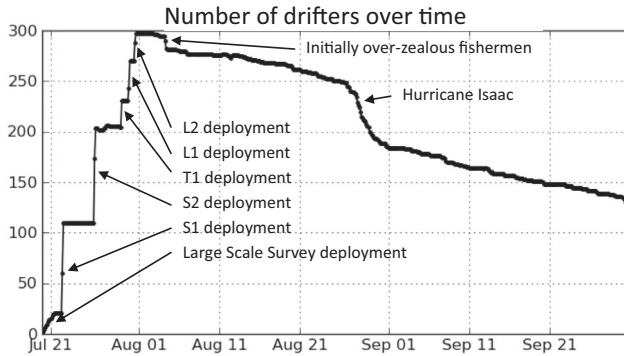


Fig. 3. The number of actively reporting GLAD surface drifters each day during the experiment. The initial deployment events are noted as well as significant events that resulted in drifter loss. Slow degradation over time is the result of limited battery life.

tially deforming the LCE front, and the FC and SC eventually merge. Northeast of the SC, an anticyclone (AC) is situated over the Florida shelf within the area from the 500 m to 100 m isobaths. During August, between the SC and AC along the 1000 m isobath, the flow to the northwest turns along the edge of the DeSoto Canyon to the southwest. Progressing through September, this northwestward flow moves into deeper waters impinging on the DeSoto Canyon and turning to join the westward coastal flow.

Development of the drifter sampling of the features is shown in Fig. 5. The S1 drifters advect slowly to the southwest initially and then flow to the east between the FC and LCE. The drifters become widely dispersed in September flowing back to the northwest. S2 initially straddles a separatrix with the western half of the drifters in the Mississippi River freshwater outflow (observed by the deploying ship) moving toward the south and southwest through the DeSoto Canyon and then to the east along the LCE. These drifters meet a bifurcation point at 26.7°N 85.7°W (noted in Fig. 4) with the majority turning northwest and the remainder turning southeast. The eastern half of S2 rapidly flows southeastward into the SC. This flow brings the S2 drifters very close to the LCE front on August 1. On August 8, the eastern S2 drifters move to the northeastern side of the SC. By August 15, the AC entrains the eastern S2 drifters, which then move closer to the Florida coast, and these persist in the northeastern region throughout September. Most of the L1 and L2 drifters are initially entrained in the FC. Once the FC and SC merge, the L1 and L2 drifters cover a large area in the southeastern quadrant of the area in Fig. 5. The L1 and L2 drifters gradually then flow back to the northwest. The T1 drifters move southwest through the DeSoto Canyon and entrain along the front between the merged FC, SC and the LCE.

4. Assimilation experiments

4.1. General system setup for experiments

The assimilation experiments are based on the forecast system using NCOM with the 3DVar in NCODA, which are the operational

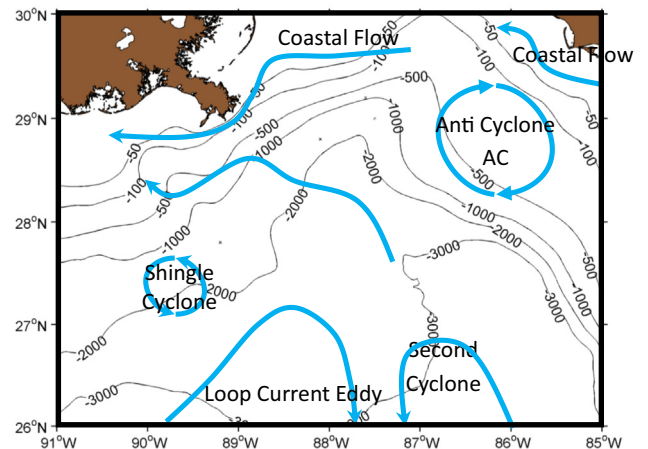
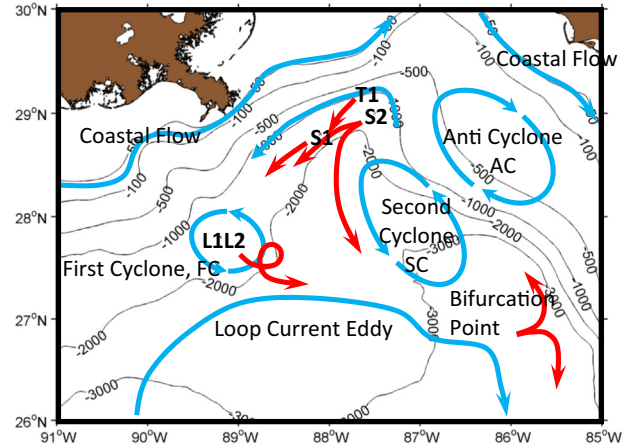


Fig. 4. General circulation features (blue lines) during August 2012 (top) and September 2012 (bottom) with initial positions of the intensive GLAD drifter deployment locations (S1, S2, T1, L1 and L2) and initial drift directions (red lines). The bifurcation point is first reached by S1 on August 31, 2012. During September the drifters are widely distributed.

systems run at the Naval Oceanographic Office for high resolution areas nested in the global system. The domain is the entire Gulf of Mexico at 3 km horizontal resolution and 50 vertical levels. Thirty-four sigma coordinates are used above 550 m depth, and sixteen Z level coordinates are used below. The sigma coordinate structure has higher resolution near the surface with the surface layer having 0.5 m thickness. Atmospheric forcing is taken from the Coupled Ocean Atmosphere Mesoscale Prediction System (COAMPS) (Hodur, 1997), and boundary conditions are from the global NCOM (Barron et al., 2004, 2006). Typically, altimeter SSH from Jason-1, Jason-2, and CryoSat-2 arrive with 24- to 48-h latency, the difference between observation time and the assimilation time. The experiments here are run in hindcast, which is different from experiments run in real time during GLAD in that the data latency is not an issue.

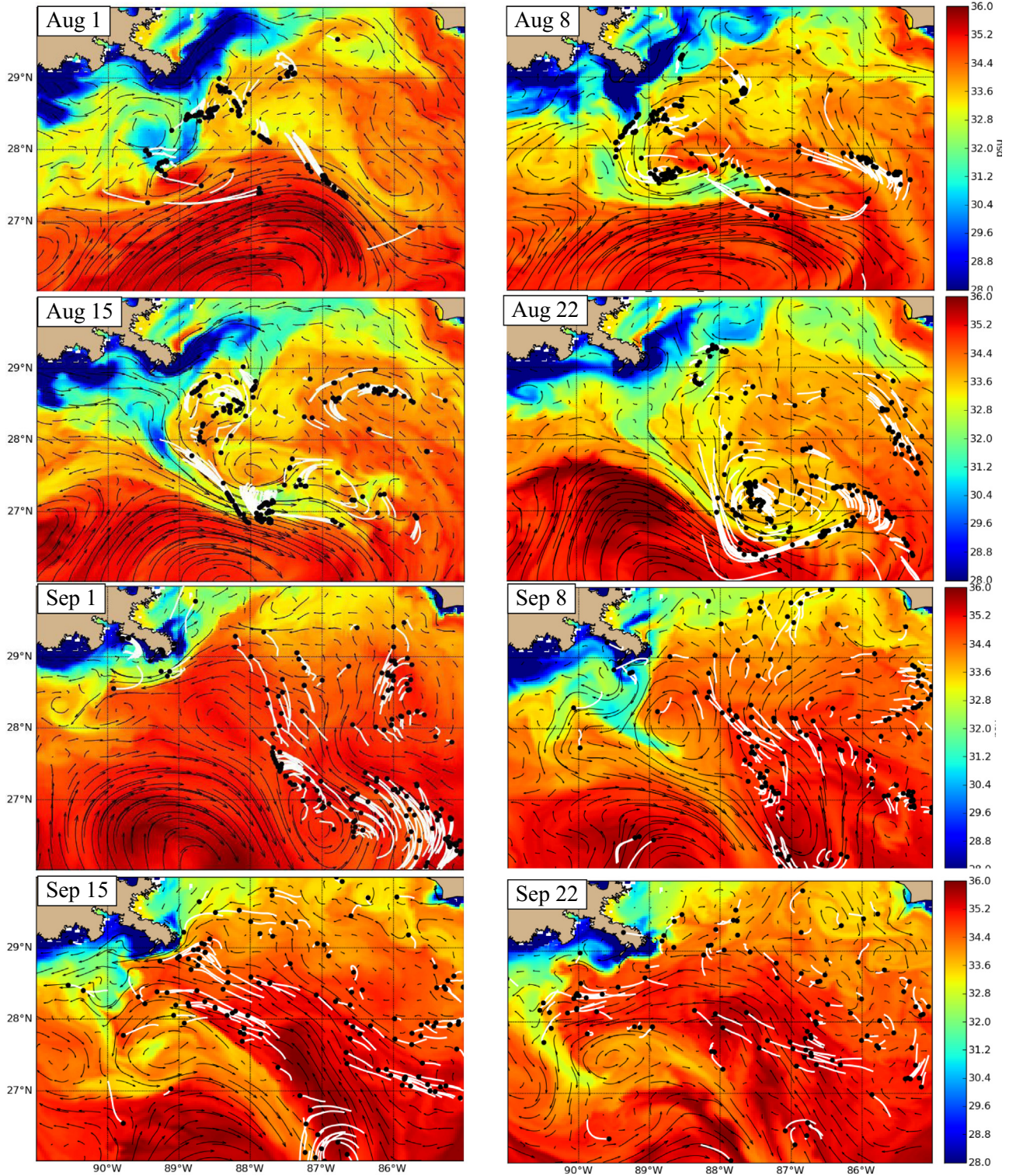


Fig. 5. Distribution of GLAD drifters through August and September. The drifter tails indicate the positions over the prior 2 days. The background color is the model sea surface salinity, and the black vectors are the model surface velocity. The model results are from experiment B6, which has the lowest errors in magnitude of velocity differences. Colorbar ranges are in Practical Salinity Units.

The satellite altimeter SSHA is the dominant information source for constraining the mesoscale field. Altimeter-observed SSHA is used with the MODAS vertical covariance information (Fox et al., 2002) to construct a synthetic temperature and salinity profile, and the synthetic profile is used in the 3DVar assimilation. All available in situ data are also used in the experiments, though

there is typically very little information providing synoptic mesoscale structure from in situ data.

The system runs a daily cycle of assimilation and forecast. All observations within the data time window T_{obs} prior to the 00Z analysis time are analyzed through the 3DVar to produce an analysis increment, which is added to the model system during an

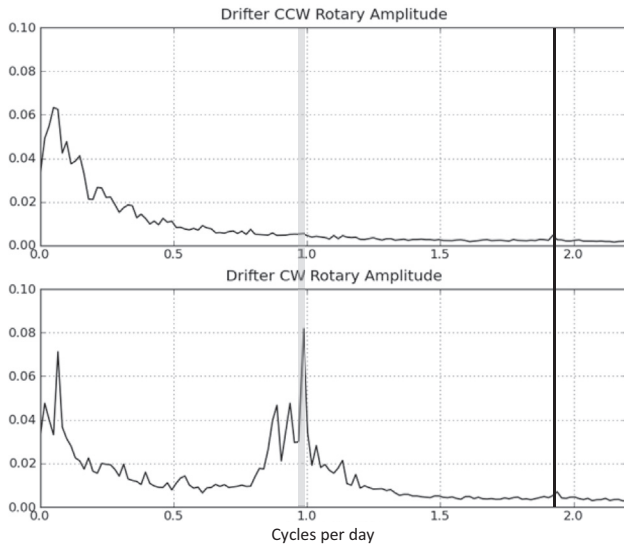


Fig. 6. Counterclockwise (top) and clockwise (bottom) rotary amplitude spectra. The rotary amplitude squared spectra are computed independently for each drifter, averaged over all drifters, and the square root is plotted. The vertical line across the two plots is the M2 (1.93 cpd) frequency. The grey vertical grey bar (0.91–0.98 cpd) is the inertial oscillation range between 27 and 29°N.

increment insertion interval T_{ins} . This interval is 6 h for all experiments except for B2, which uses 24 h. The system divides the 3DVar analysis increment by the number of time steps in the insertion interval, and at every model time step the fractional increment is added to the state. Note that the data time window T_{obs} and incremental insertion interval T_{ins} represent the time correlation of the assimilation system. Adding the analysis to the initial condition represents a time correlation function that is a Dirac delta in time, which is physically unrealistic. Previous experiments show that changing only the initial condition results in transient waves and oscillations that can persist for several days in the ocean, and these transients do not appear when the 6 h incremental insertion interval is used. The incremental insertion interval represents a boxcar correlation over time with a value of $1/T_{ins}$ over T_{ins} and 0 elsewhere. Extending the data time window T_{obs} beyond 1 day results in observations correcting errors with time scales longer than 24 h.

4.2. Particular assimilation experiments

The assimilation experiments individually perturb different assumptions within the background error covariance function. The 3DVar estimates the analysis increment $\delta\mathbf{x}$, which is an optimal correction to a background \mathbf{x}_b given by the deceptively simple equation (Daley and Barker, 2001):

$$\delta\mathbf{x} = \mathbf{P}_b \mathbf{H}^T [\mathbf{H} \mathbf{P}_b \mathbf{H}^T + \mathbf{R}]^{-1} [\mathbf{y} - \mathbf{H} \mathbf{x}_b] \quad (1)$$

where \mathbf{P}_b is the error covariance of the background state \mathbf{x}_b , \mathbf{H} is an operator that maps the background state to observations \mathbf{y} , and \mathbf{R} is the observation error covariance.

A history of research into \mathbf{P}_b exists both in methods for specifying an analytic functional form and in the numerical solution process. The mathematical foundation of the convolution integral (Gaspari and Cohn, 1999), solution through an implicit diffusion operation (Carrier and Ngodock, 2010) and generalized extensions of the Gaussian diffusion operation (Weaver and Mirouze, 2013) work to provide state covariance relations and efficient solutions based on historical observations or heuristic arguments of scales

of processes such as the Rossby radius of deformation (Cummings, 2005).

The 3DVar here uses the approach of Brandt and Zaslavsky (1997) to initially separate \mathbf{P}_b into variance \mathbf{S}_b and a correlation function \mathbf{C}_b as $\mathbf{P}_b = \mathbf{S}_b^{1/2} \mathbf{C}_b \mathbf{S}_b^{1/2}$. A decomposition of \mathbf{C}_b into separable functions is then made:

$$\begin{aligned} \mathbf{C}_b(x, y, z, t, v, x', y', z', t', v') \\ = \mathbf{C}_{hb}(x, y, v, x', y', v') \mathbf{C}_{vb}(z, v, z', v') \mathbf{C}_{fdb}(x, y, v, x', y', v') \end{aligned} \quad (2)$$

The correlation between two variables v and v' , at horizontal locations x, y and x', y' , and vertical positions z and z' is the product of the separable components of horizontal \mathbf{C}_{hb} , vertical \mathbf{C}_{vb} and flow dependent \mathbf{C}_{fdb} correlation functions. This separation of variables is relatively typical since there is not sufficient a priori information to provide the full space-lagged correlations between all variables as the relations change throughout the globe. Such decomposition is applied in general circulation models (Derber and Rosati, 1989), the Harvard Ocean Prediction System (HOPS) (Lozano et al., 1996), MERCATOR (Brasseur et al., 2005), the Forecasting Ocean Assimilation Model (FOAM) (Martin et al., 2007) and the Climate Forecast System (CFS) reanalysis (Saha et al., 2010). Because \mathbf{P}_b is a strong controller of the solution, additional approaches for its specification are considered, and these are discussed further in Section 6.

The vertical correlations \mathbf{C}_{vb} are computed using a Gaussian function with length scales based on the density gradients of the background profile. Note that we do not test perturbations of the vertical correlations. The altimeter observations are used in conjunction with the correlations based on historical in situ profiles to estimate synthetic temperature and salinity profiles that are subsequently provided to the assimilation. The correlations change bi-monthly and spatially. Thus, the assimilation process uses synthetic profiles that have the historically observed vertical correlation impressed on them. The vertical correlations in the assimilation will tend to smooth the synthetic profile vertical gradients. Formally, the vertical correlations in \mathbf{P}_b should be based on the observed correlations rather than constructing synthetic profiles prior to the assimilation. Since the synthetic profiles are based on historical data, we believe these have the least probability of error, and we have no other proposed superior source on which to test.

Horizontal correlations \mathbf{C}_{hb} are computed using a second order auto-regressive function (SOAR) (Gaspari and Cohn, 1999) with a length scale based on the Rossby radius of deformation, and a geostrophic coupling component is included to relate velocity and geopotential height. Thus, the analysis is in geostrophic balance. The flow-dependent correlations are $\mathbf{C}_{fdb} = (1 + s_f)e^{-s_f}$, where, $s_f = \delta(\text{SSH})/dh$, $\delta(\text{SSH})$ is the difference in model forecast SSH between two observation locations, and dh is the specified flow dependence scale factor, which is expressed in centimeters. This increases the correlations between points that have little SSH difference and decreases correlation across SSH gradients. The SSH field is used in the flow dependent correlation under the assumption that the flow is in geostrophic balance and directed along pressure surfaces due to mesoscale features. Obviously some processes such as tides are not aligned with this assumption. However, spatial scales for tides are typically well separated from the mesoscale in the deep ocean. Thus it is not expected to be a significant problem. The flow field itself could be used in the formulation, though some influence of the tidal signal would still contribute.

The 3DVar approach assumes all observations occur at the analysis time, and thus time is not explicitly stated in Eq. (1). Time scales in the ocean are long, and attempts to take the time correlation into account mainly consist of including observations over a data window T_{obs} that is long. MERCATOR assimilates altimeter

data covering the prior 7 days in an assimilation cycle that occurs every 7 days, FOAM has a daily assimilation cycle with data used over multiple cycles and an error variance increasing linearly with data age, the Bluelink Ocean Data Assimilation System (BODAS) (Oke et al., 2008) uses an 11-day T_{obs} to assimilate observations and CFS conducts a 6 h assimilation cycle using data in the prior 10 days with a weighting based on data age. Cummings et al. (2009) use a 1-day T_{obs} and daily assimilation cycle. Formally, observations should be assimilated only once. Otherwise observation error variances are not accurate. A long time between assimilation cycles implies that new data could improve the forecast but is not having an impact. While a one day assimilation cycle does use newly acquired observations, it does not allow a long time period correlation. Thus, consideration of the observation time window also is an open question to be addressed.

To determine the impact of the background error covariance components, one experiment is run for each postulated error source with changes in the system relevant for testing the specific sensitivity. The independent changes allow the results to be interpreted more easily. The main parameter settings are summarized in Table 2.

For the first set of experiments (denoted with R for the first set of runs), details in the error variance amplitude formulation, horizontal correlation scale, the flow dependence, the data time window and the incremental insertion interval are as follows:

R1: This run is set up identically to the experiment run in real time during the GLAD deployment, though data latency is not an issue. All subsequent experiments in the first set are deviations from this initial experiment. The data time window T_{obs} includes all observations obtained within the prior 24 h, and the analysis increment insertion interval T_{ins} is 6 h. Horizontal correlation scales are on average 21.2 km. The background error variance is a function of spatial position including horizontal and vertical. It is computed based on changes in the 24 h forecast state over the prior 10 analysis cycles. Given a 24 h forecast \mathbf{x}_i^f from prior cycle i , we calculate the weighted average of squared differences $\sum_{i=1}^{10} w_i (\mathbf{x}_i^f - \mathbf{x}_{i-1}^f)^2$ which is the weighted sum of squared differences the 24 h forecast ocean state from different forecast cycles (i and $i-1$), where the weights w_i are given by Cummings and Smedstad (2013). Areas in which observations produce large differences between two forecasts result in larger variances. This is an advantage to the algorithm as errors are based on observation impact to the forecast. In areas that are not observed for some time, the main contributor to the background error variance results from model time-variability. This is a drawback due to the sparse sampling of the

ocean in which areas unobserved for some time result in small differences between background and analysis. Thus, an underestimation of error variance is expected.

R2: If the background variance amplitude \mathbf{S}_b is too small, the analysis may favor the background over the observations, so we test a second error variance estimation approach in R2. At the conclusion of each analysis, the forecast error variance \mathbf{S}_f is computed, and this becomes the background error variance for the subsequent cycle. The forecast error variance in R2 is computed through four contributions:

$$\begin{aligned} \mathbf{S}_f = & \left(\mathbf{I} - \left(\mathbf{H}^T \mathbf{P}_b \mathbf{H} + \mathbf{R} \right)^{-1} \right) \mathbf{S}_b + \gamma^f \sum_{i=-10}^1 w_i (\mathbf{x}_i^f - \mathbf{x}_{i-1}^f)^2 \\ & + \gamma^a \sum_{i=-10}^0 w_i (\delta \mathbf{x}_i)^2 + \gamma^c (\mathbf{S}_c - \mathbf{S}_b) \end{aligned} \quad (3)$$

During the analysis cycle, we compute the formal error variance reduction given by $\left(\mathbf{I} - \left(\mathbf{H}^T \mathbf{P}_b \mathbf{H} + \mathbf{R} \right)^{-1} \right) \mathbf{S}_b$, which accounts for the observation distribution and observation errors, and this provides the error variance at analysis time. To represent error variance at the subsequent analysis time, this variance must increase. Three sources of error growth are sequentially added to produce the forecast variance amplitude.

The first error growth source is the same as in R1 and is added with a timescale $\gamma^f = 1/2$. The second growth estimate is given by $\gamma^a \sum_{i=-10}^0 w_i (\delta \mathbf{x}_i)^2$, where $\delta \mathbf{x}_i$ is the analysis increment provided by (1) from the prior assimilation cycle i , and w_i are weights equal to those in the first term. This accounts for the recent history of forecast error measured by observations. This estimate is added to the forecast error with $\gamma^a = 1/10$. Note, this estimate is similar to the estimate in R1 in that it can only be non-zero where the ocean is observed, and this contribution to the algorithm only affects areas with recent observations. The third error growth is given by $\gamma^c (\mathbf{S}_c - \mathbf{S}_b)$, which compares the climatological variability \mathbf{S}_c stored in the Generalized Digital Environmental Model (GDEM) database (Carnes et al., 2010) with \mathbf{S}_b , and we increase the forecast error toward the climatological estimate with $\gamma^c = 1/20$. This value generally provides an upper limit on variance amplitude in the thermocline in the absence of observations. In practice, the final forecast variance amplitude shows the desired behaviors: the forecast error estimate is reduced where observations have corrected the model state, in areas with observations it is consistent with background minus observation differences, and it increases toward a climatological estimate as the ocean is not observed for days to weeks. This forecast error variance amplitude is

Table 2

The parameters for the model experiments are noted. The background error variance formulations used in the experiments are denoted as R1 or R2, as described in the text. A smaller flow dependent scale factor results in smaller horizontal correlation scales perpendicular to the flow and longer ones parallel to the flow. The data time window is the period relative to the analysis time over which observations are included in the analysis. The increment insertion interval is the time period during a hindcast over which the analysis increment is added to the system.

Experiment	Background error variance	Average horizontal correlation scale (km)	Flow dependent scale factor dh (cm)	Data time window T_{obs}	Increment insertion interval T_{ins} (h)
R1	R1	21.2	12	–24 to 0 h	6
R2	R2	21.2	12	–24 to 0 h	6
R3	2 * R1	21.2	12	–24 to 0 h	6
R4	R1	12.6	12	–24 to 0 h	6
R5	R1	21.2	12	–7 to 0 days	6
B1	R2	21.2	6	–7 to 0 days	6
B2	R2	21.2	6	–7 to 0 days	24
B3	R2	12.6	6	–7 to 0 days	6
B4	R2	38.5	3	–7 to 0 days	6
B5	R2	21.2	6	–14 to 0 days	6
B6	R2	21.2	6	–7 to 0 days	6
B7	R2	21.2	6	–7 to +7 days	6

the background error variance amplitude for the subsequent analysis cycle. The parameters of Eq. (3) γ^f , γ^a and γ^c can be optimized through either a forward perturbation or inverse estimation approach. Positive results here indicate increased skill using the new formulation, and thus it would be valuable to determine optimal settings of the parameters in the future.

R3: As a reference between the background error covariance of R1 and R2, this experiment uses an error variance double that of R1. This background error variance is larger than R1 though still much smaller than R2. The results of this experiment do not produce significant improvements.

R4: The LCS results (Fig. 1) indicate that the spatial scales of model features are relatively large compared to those in the satellite observations. Reducing the horizontal correlation scale to 12.6 km is proposed for the assimilation system to represent the smaller scales appearing in the satellite altimeter data. The results indicate this did not provide a substantial effect.

R5: This experimental case lengthens the data time window T_{obs} to 7 days. In many prior marine rapid environmental assessment exercises, the first step is to conduct a precursor large area survey to provide a large domain snapshot of dominant regional features used to initialize forecasts (Leslie et al., 2008; Gawarkiewicz et al., 2011; Lermusiaux, 2002). These surveys are repeated on a regular basis throughout the full experiment period alternating with adaptive surveys targeting the local features of interest. Operators required accurate local features determined by a full range of multiple dynamical scales. Assimilating only small isolated information is not sufficient for forecasts from local model nests to be dynamically balanced with the surrounding larger scale features (Robinson, 1997). Thus, broad information is also required. On a daily basis, very isolated lines are observed by satellite in the Gulf of Mexico. Initialization of the Gulf of Mexico model using a wide area ship synoptic survey is not feasible. However, during a 7 day period, satellite altimetry provides wide coverage of the Gulf and could be used to produce a fuller domain picture. Given these considerations, instead of using the 24 h of data as in R1, 7 days of data could provide more complete information on the larger scale quasi-synoptic structure. Since the observation error levels are not changed from R1, the repeated use has the detrimental result of effectively increasing data weight. This limitation may lead to some distortions of the local dynamical features and is addressed later in experiment B6.

Comparison of the LCS from the first set of experiments shows a better qualitative match with the chlorophyll patterns in R5 (Fig. 7). To compute the LCS we adopt Haller and Beron-Vera's (2012) proposed geodesic theory. This theory leads to (attracting) LCS at any time t_0 as locally minimally stretching strainlines obtained from a backward flow computation from t_0 to $t_0 - T, T = 30$. Such strainlines are (material) curves tangent to the contractional eigenvector field of the Cauchy–Green strain tensor, given by $C_{t_0}^{t_0-T}(x_0) = [dF_{t_0}^{t_0-T}(x_0)]^* dF_{t_0}^{t_0-T}(x_0)$. Here x_0 is the position of a fluid particle at time t_0 and $F_{t_0}^{t_0-T}(x_0)$ is the deformation tensor at the particle position at time $t_0 - T$, which follows from solving the fluid particle motion equation $\dot{x} = v(x, t)$, where $v(x, t)$ is the fluid velocity field, and the asterisk represents a conjugate transpose.

The analysis of this first set of experiments is discussed in Section 5. The results indicate that the background error variance of experiment R2 provides improvement. Comparison to chlorophyll suggests an improvement in direction of currents in experiment R5, and the implication is that there is a long time correlation in

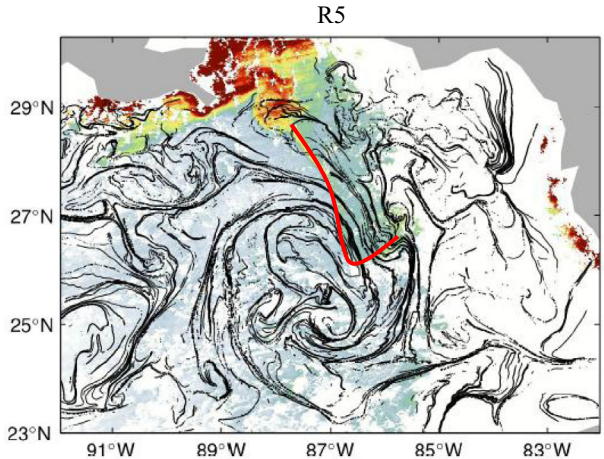


Fig. 7. LCS structures from the experiment R5 superimposed on MODIS chlorophyll image on July 12, 2012. The change in the data time window T_{obs} in R5 produces the best agreement from the first set of experiments. The red line is the same as in Fig. 1, which is used to identify the chlorophyll core.

the background errors that should be addressed. However, drifters suggest experiment R5 contains shortcomings in the magnitude of the currents. Based on this, a second set of experiments is defined denoted with a B as the second set of runs:

B1: This is a combination of the modified background error variance used in R2 and the lengthened data time window of R5 using the 7 day data time window. All subsequent experiments in this second set are a perturbation from this reference. The flow dependent scale factor dh is decreased in the B experiments, which results in increasing observation correlation in the direction of constant geopotential and decreasing correlation in the perpendicular direction.

B2: This is the same as B1, except that the increment insertion interval T_{ins} is increased from 6 h to 24 h. Using a 24 h interval would be expected to produce more realistic correction to the background state, though a shorter increment insertion interval requires less hindcast time. Thus, there is motivation to reduce the increment insertion interval from the computational cost perspective. Results show this parameter has a negligible effect.

B3: The horizontal correlation scale is again tested in combination with the long time data window by reducing the value to 12.6 km.

The results again did not show significant improvement.

B4: The horizontal correlation scale in the direction of constant surface geopotential is increased in this experiment by changing the flow dependent scale factor dh and changing the horizontal correlation scale. The flow dependent scale factor increases horizontal correlation scales in the direction of the constant geopotential and decreases scales in the direction perpendicular. At the same time, the horizontal correlation scale is increased to 38.5 km. The result of these two effects is to maintain the same horizontal correlation scale perpendicular to the flow and greatly extend the horizontal correlation scale parallel to the flow. The purpose is to extend observation influence further in the direction of flow. This experiment did not result in a positive improvement.

B5: This experiment doubles the data time window to 14 days from the 7 days used in B1. The results do not demonstrate increased skill.

B6: Experiment B1 uses observations multiple times because of the 7-day data time window, and this process is formally incor-

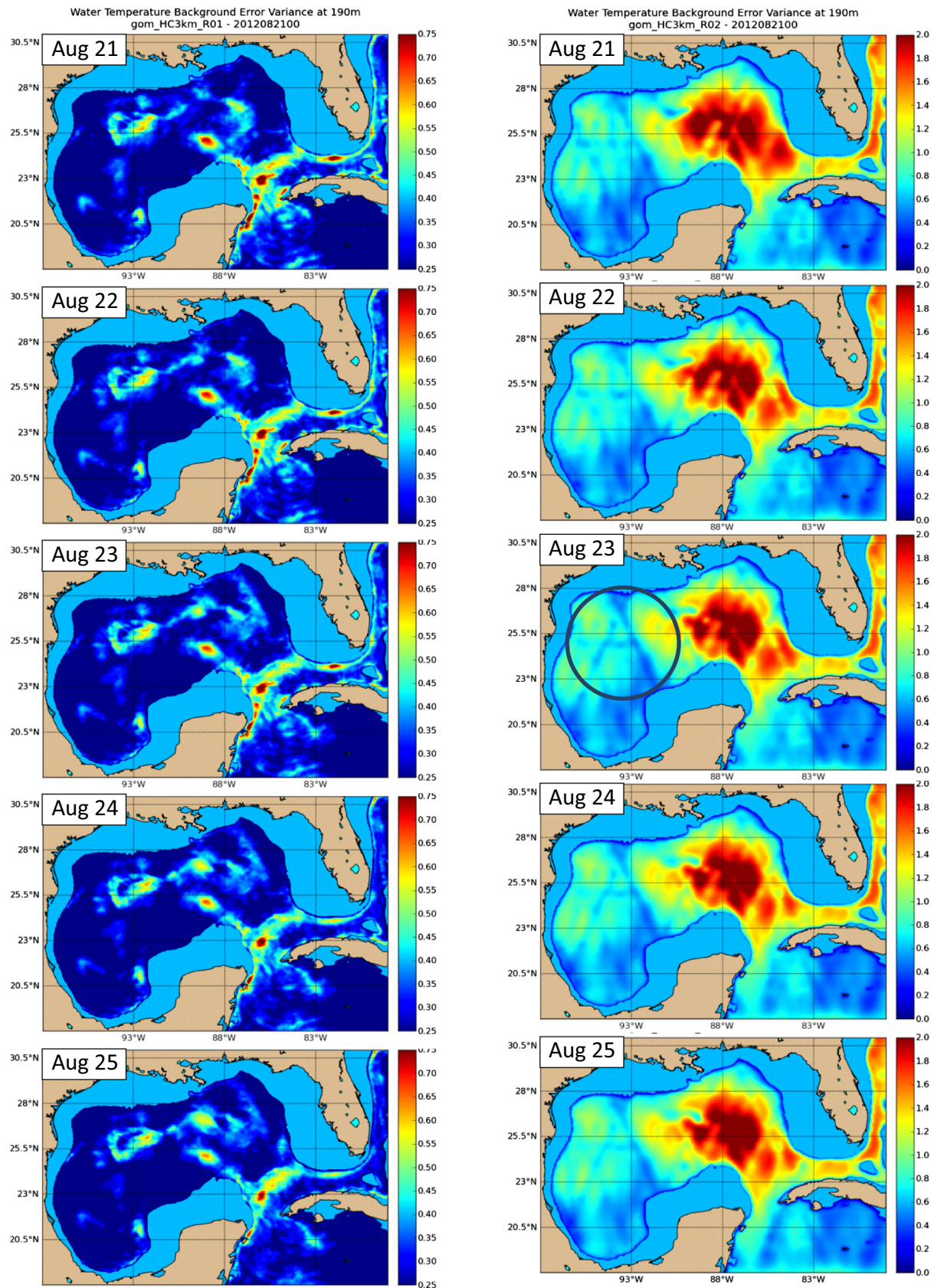


Fig. 8. Background error standard deviation S_b of 190 m temperature on 2012 August 21 through 25 (top to bottom rows), from experiments (left) R1 and (right) R2. The circled area indicated on August 23 contains reduced variance from observations on August 22 (Fig. 10). Note the different colorbar ranges for R1 (0.25–0.75 °C) and R2 (0–2 °C).

rect. Given the observation error levels, using observations more than once results in the solution matching the observations more than it should, and the analysis is more susceptible to noise in the data. A correct method to use observations once and provide a long time correlation would be to use a data time window of 1 day and extend the incremental insertion interval over multiple days. As previously discussed, the system divides the analysis increment by the number of time steps in the increment insertion interval. Thus the difference between inserting over one day and inserting over 7 days is dividing the analysis increment by a factor of 7. This experiment is the same as B1 (daily cycling with a 7 day data time window and 6 h incremental insertion interval) with the exception that the analysis increment is divided by the number of days in the data time window. This is intended to emulate using observations in one analysis with an analysis increment insertion interval of 7 days with a correlation that is constant in time throughout the 7 days. This is not an entirely correct emulation since the analysis increment influence of single observations changes from one day to another as the background, and thus observation minus background changes.

B7: As a reanalysis, it is possible for data in the future to affect the analysis time as well as data in the past. This experiment uses a data time window that is -7 days to $+7$ days relative to the analysis time. Results did not indicate a significant benefit.

5. Results

5.1. Background error variance amplitude and time correlation

The background error variance amplitude \mathbf{S}_b formulation is a strong controller of the solution. Fig. 8 provides a comparison of \mathbf{S}_b over several days computed by the error variance formulations in R1 and R2. The amplitudes are roughly a factor 5 larger in R2 compared to R1 (note different colorbar ranges in Fig. 8 for R1 and R2). The estimated error variance amplitude \mathbf{S}_b is evaluated relative to the observed errors in the background field ($b - o$). At each depth d , with N_d subsurface observations during the experiment, an estimate of background error variance in temperature $\widehat{\mathbf{S}}_d$ is computed as

$$\widehat{\mathbf{S}}_d = \frac{1}{N_d} \sum_{i=1}^{N_d} (b_{d_i} - o_{d_i})^2 \quad (4)$$

where the background field is interpolated to the observation location. For comparison, the estimated background error variance \mathbf{S}_b in experiments R1 and R2 are sampled at the observation locations and averaged over the experiment time. Fig. 9 compares the square root of the error variance from R1 and R2 to the estimate $\widehat{\mathbf{S}}_d$. The variance values of \mathbf{S}_b should be less than those of $\widehat{\mathbf{S}}_d$ since observation representation errors and noise contribute to $\widehat{\mathbf{S}}_d$ in addition to the background errors. Fig. 9 shows the \mathbf{S}_b in experiment R2 is a better representation than experiment R1 when compared to observation minus background variance at most depths. The typical thermocline and halocline depths are about 200 and 250 m respectively in the eastern Gulf of Mexico. Results from R2 indicate the background error variance \mathbf{S}_b computed by the algorithm in Eq. (3) provides a good representation of the estimated $\widehat{\mathbf{S}}_d$, though the algorithm provides a slight over estimate. One reason for the apparent over-estimation may be that the observations are mainly the synthetic profiles generated from the altimeter data. The synthetic profiles will contain less variance than real profiles.

The R2 increment fields (Fig. 10) reflect the location of satellite tracks. In R2, the background error variance reduction based on observation locations and error levels is computed and subtracted from \mathbf{S}_b , and then the error growth terms are added according to

(3). This becomes the background variance for the successive analysis cycle on the next day, so that observation impacts on \mathbf{S}_b are seen in the background variance on the following day. One example is indicated by the circles in Figs. 8 and 10. On August 22, observations over the western Gulf of Mexico (Fig. 10) produce background error variance reduction on August 23 (Fig. 8). The background error variance on successive days (Fig. 8) shows the impact of relaxing toward climatological variability in areas that have no observations as the error variance under prior observations gradually increases.

The second important factor is the correlation time scale of the background errors. The increments are compared between R2 and B1 (Fig. 10), which both use the same \mathbf{S}_b . B1 has a 7 day data time window vs. 1 day for R2. For example, on August 21 there are increments along the satellite track transiting from 20.5°N 83°W to 30.5°N 86°W (encompassed by the box in Fig. 10). In experiment R2, the increments occur along this track only on August 21. In experiment B1, the increments appear on August 21, and subsequent days also show the increments with amplitude diminishing in time over 3–4 days. If background errors are not correlated over long times, the second use of the data would have a much smaller increment and the increment would be more noise than signal. Additionally, the increments in the case of B1 are generally smaller than the increments due to the same data in R2, indicating the background field is closer to the observations in B1.

The increment fields on August 21 of experiments B1–B7 (Fig. 11) indicate the effects of the increment insertion interval (B2), the flow dependent correlations (B3 and B4), the data time window (B5 and B7), and emulating the long time correlation (B6). The main improvement relative to the drifters occurs in B6 in which the analysis increments are divided by the data time window resulting in much smaller values.

5.2. Evaluation through GLAD observations

The unassimilated GLAD drifters serve as independent evaluation data. Each experiment is sampled at the latitude and longitude location of each drifter. The velocity vectors are computed every 3 h, resulting in over 100,000 observations. The 3-h sampling observes the same mesoscale eddies for quite some time, thus the number of independent observations is not the same as the number of observations. The drifters do cover a wide range of different eddies and associated fronts during the deployment time

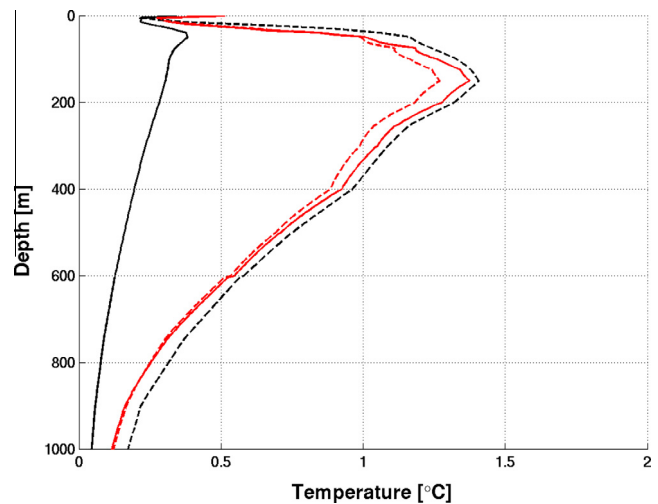


Fig. 9. Square root of the specified background error variance averaged over all observations during the experiment from R1 (solid black) and R2 (dashed black) compared to the RMS difference of observations minus background from R1 (solid red) and R2 (dashed red).

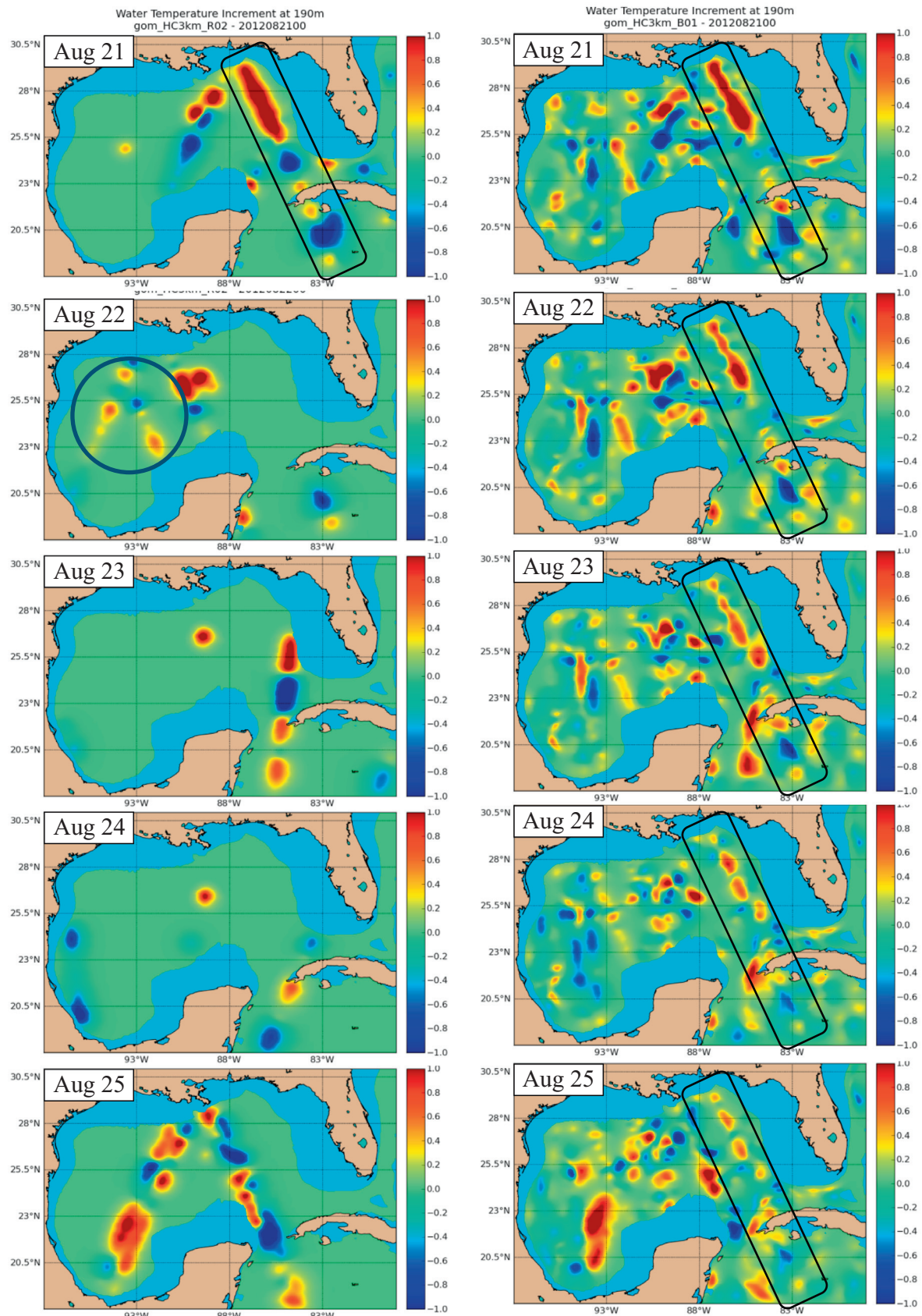


Fig. 10. Analysis increments on August 21 through 25 2012 (top to bottom rows) for (left) R2 with a 1 day data time window and (right) B1 with a 7 day data time window. Highlighted areas are discussed in the text. These are the corrections to the model state computed by the 3DVar system. Colorbar ranges are in °C.

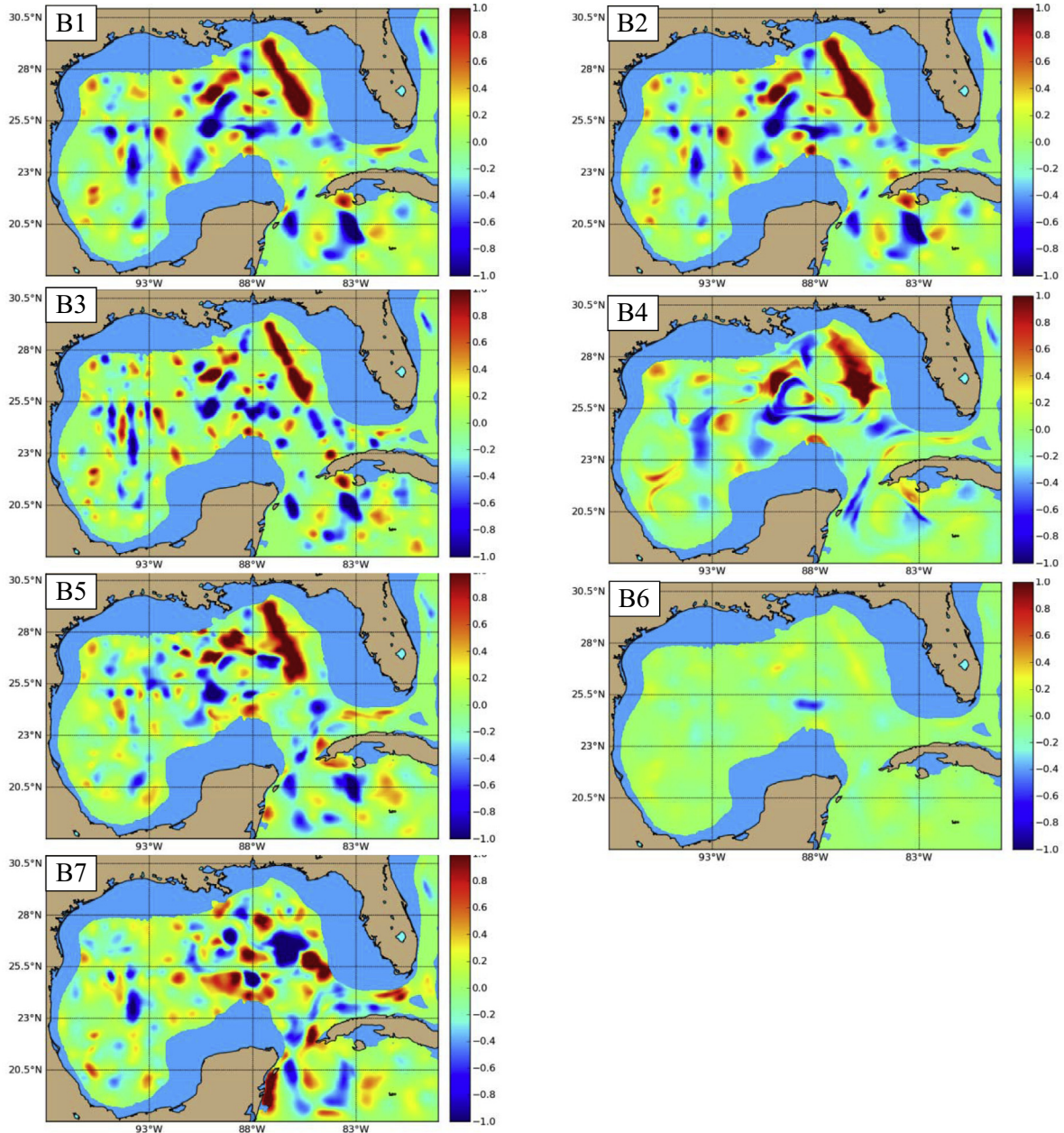


Fig. 11. Analysis increments on August 21, 2012 from experiments perturbing properties relative to B1 including: increment insertion interval (B2), the flow dependent correlations (B3 and B4), the data time window (B5 and B7), and emulating the long time correlation (B6). Colorbar ranges are in °C.

period (Fig. 5), thus the number of independent observations is high during the 60 day experiment period.

An initial comparison is made through the rotary coherence and phase difference spectra (Fig. 12). The model experiments indicate high coherence over the mesoscale band from 0 to 0.75 cpd in both clockwise and counterclockwise spectra with a phase difference between $\pm 20^\circ$. Typically, R2 has higher coherence than R1 in this band, R5 is lower than R1, and B6 is near the top coherence. As a reference, geostrophic currents from the AVISO sea surface height maps are computed, and the statistics for these currents are also presented in Fig. 12 and subsequent analyses.

The inertial oscillations in the 0.9–1.1 cpd range in the clockwise spectra show high coherence in the models, though phase differences are higher. The inertial oscillations are typically forced by surface wind stress events. The accuracy in the inertial band is a measure of wind forcing accuracy and dynamical system response in the surface layer. In addition, coherence is high at the

semidiurnal frequency just below 2.0 cpd, and this is due to tidal forcing at the boundaries and tidal potential forcing in the interior.

The high frequency (greater than 0.75 cpd) response is primarily a forced response, and the interest at hand is in the low frequency response that is affected by the assimilation process. To focus on this variability, model velocities are interpolated through a bilinear interpolation to the latitude and longitude locations of the drifters. Then, all the time series of velocities from the models and those inferred from the drifters are passed through a Butterworth filter with a 0.5 cpd cutoff. Thus the subsequent error characterizations are for the low frequency only.

Error histograms over all data are computed (Fig. 13). These are the fraction of observations within each bin treating magnitude and direction errors independently rather than binning error in the vector difference. Thus, skillful system error distributions should be clustered around 0° direction error and small magnitude error. The distribution for R1 provides the fraction of all observations that

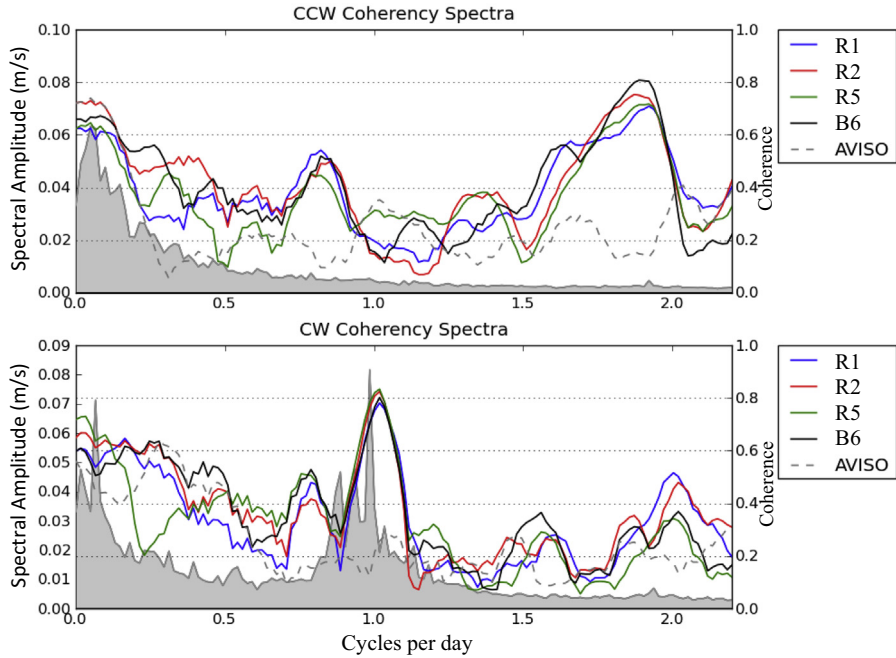


Fig. 12a. Counterclockwise (top) and clockwise (bottom) rotary coherency spectra. A filter with frequency width of 0.1 cpd is applied. The colored lines are the coherency spectra with vertical scale on the right, and the shaded background is the amplitude spectrum from the drifters as in Fig. 6 with the vertical scale on the left.

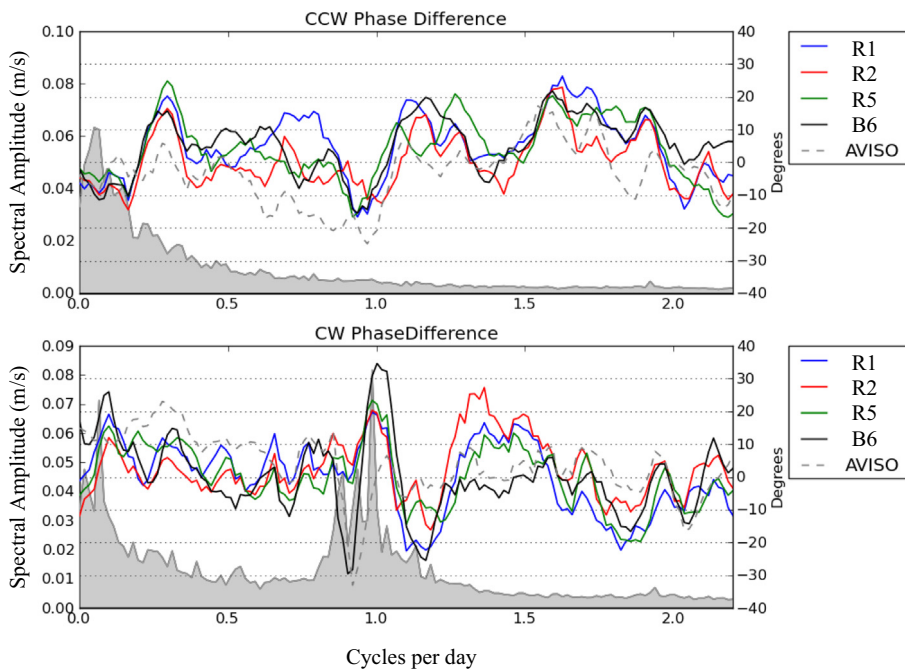


Fig. 12b. Counterclockwise (top) and clockwise (bottom) rotary phase difference. A filter with frequency width of 0.1 cpd is applied. The colored lines are the phase difference spectra with vertical scale on the right, and the shaded background is the amplitude spectrum from the drifters as in Fig. 6 with the vertical scale on the left.

fall in each (magnitude, direction) bin. The majority of errors is clustered around 0° direction and is less than 0.2 m/s. For more direct comparison, the error distribution of R1 is subtracted from the histograms computed from other experiments, and the color bar range is changed to highlight the difference in fraction of observations between the experiments and R1. Areas of blue indicate

fewer occurrences than R1, and areas of red indicate more occurrences. An experiment is performing better than R1 if there is a distribution of blue away from the center and red near the center and near 0° as in the distributions of R2 and B6.

A 16 element matrix fully describes cross correlations between observed and modeled vectors (Crosby et al., 1993), and a range of

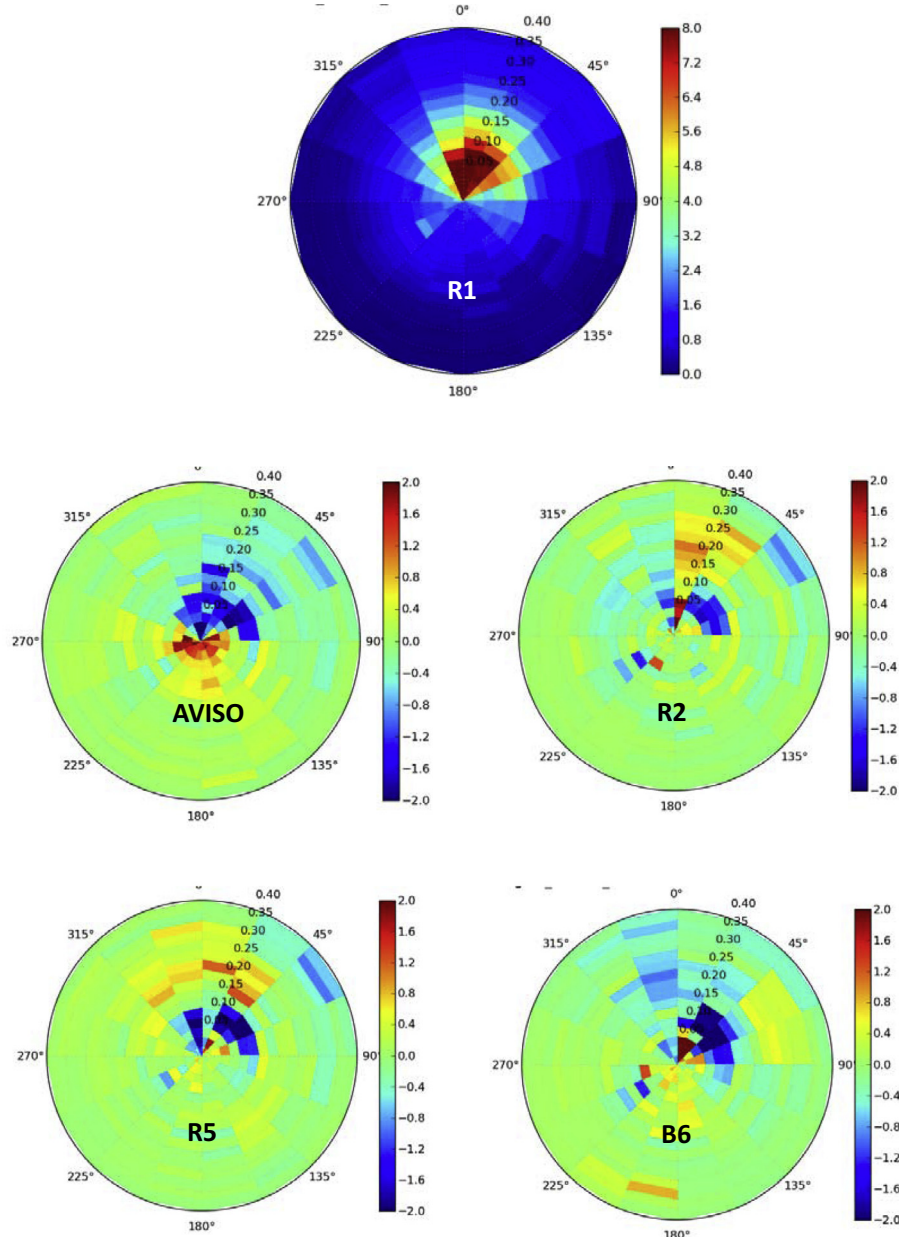


Fig. 13. Error histograms distributions relative to GLAD inferred velocity observations from R1 (top row). Skillful system error distributions should be clustered around 0° direction error (toward top of the figure) and small magnitude error. Other experiments are presented as differences in distribution minus the distribution of R1 (second row) AVISO and R2, (third row) R5 and B6. An experiment is performing better than R1 if there is a distribution of blue away from the center and red near the center and near 0° as in the distributions of R2 and B6.

statistics are proposed using subsets of these elements. To help illustrate the results succinctly, we compute cumulative distributions that show the fraction of the observations with errors less than a prescribed value. It is useful to examine these across three statistics: (1) the difference between observed and modeled magnitude of velocity vector (Fig. 14), (2) difference in direction measured in degrees (Fig. 15), and (3) the magnitude of the difference in observed and modeled velocity vector (Fig. 16). The cumulative probability distributions of errors are similar, and small differences are important. To better highlight the small differences, the cumulative distribution for experiment R1 is subtracted for each of the statistics, and the difference between R1 and each experiment is also presented in the figures. In comparing two experiments, the distributions with more occurrences at low error

values are performing better. Because these are cumulative distribution curves as a function of error level, the higher (and more positive) the curve at low error levels, the better the performance. Only the experiments that demonstrate significant impact beyond the initial experiments R1 and B1 are shown, which are R2, R5 and B6. The geostrophic currents computed from direct analysis of SSHA by AVISO are included as a reference.

R2 is performing overall better than R1 with a higher fraction of occurrences at low error levels across all statistics. This is confirmation that the S_b of R2 is a better representation than the S_b value of R1. R3, which doubles the S_b of R1, has little impact on the results. Similarly, R4, which reduces the horizontal correlation scale using the same error variance amplitude as R1, has little impact. R3 has a distribution very similar to R1, and R4 performs

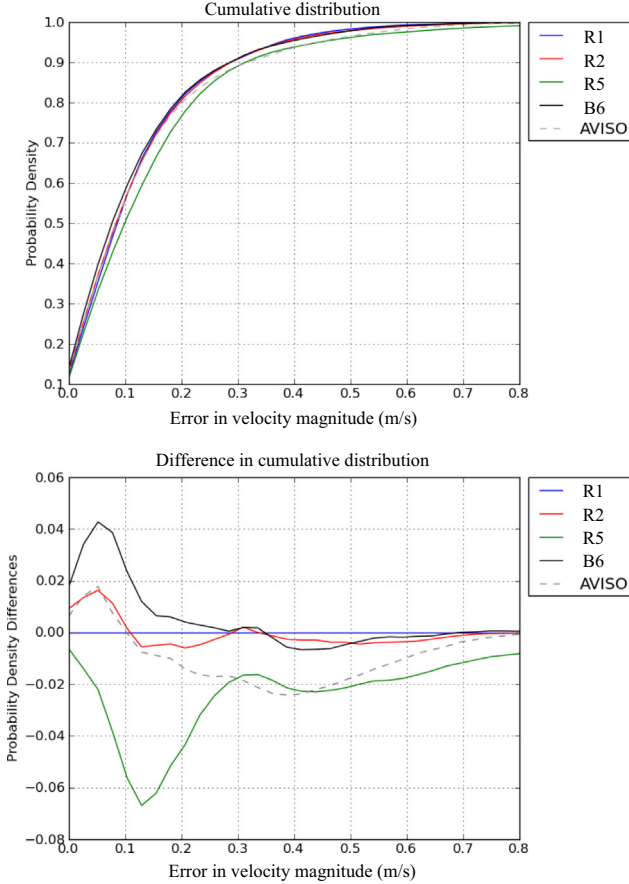


Fig. 14. (Top) cumulative distributions of the difference in magnitude of velocity from the model experiments and the GLAD drifter inferred velocities. (Bottom) to better visualize the differences, the distribution of R1 is subtracted from all the experiments. Distributions with more occurrences at low error values are performing better. Thus B6 is the best performing experiment by this metric.

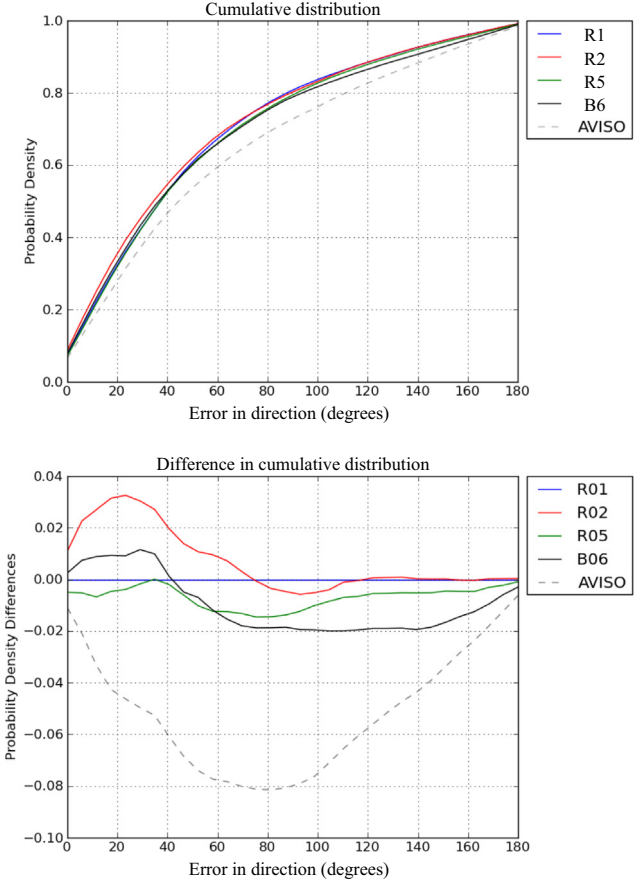


Fig. 15. (Top) cumulative distributions of the difference in direction of velocity from the model experiments and the GLAD drifter inferred velocities. (Bottom) to better visualize the differences, the distribution of R1 is subtracted from all the experiments. R2 is performing best with more occurrences at low errors. B6 is performing better than R1.

slightly worse. The cumulative distributions are not shown for these for brevity and clarity.

R5 is the first experiment to include a long data time window (7 days). Though the initial LCS comparison in Fig. 7 indicates an improved qualitative comparison relative to the advected chlorophyll, the error distribution statistics from the GLAD drifters show poorer performance than R1. The errors in magnitude of velocity are the primary cause, and this is also reflected in the magnitude of the difference between observed and modeled R5 velocities. The positive comparison to the chlorophyll distribution points out the risk involved in evaluations based on a small sample set or metric, which represents one instant in time and only an evaluation of flow direction compared to the chlorophyll.

The comparison between R2 and B1, which both use the same S_b but have different data time windows (Fig. 10) implies that background errors are correlated in time. This should be expected. Many estimates of the error covariance structure start with the assumption that the scales of the errors are on the order of the scales of the features themselves. The ensemble optimal interpolation of BODAS (Oke et al., 2008) uses ocean model ensembles to build the spatial covariance relations. The 11-day assimilation cycle of this system also points to the use of a long data time window. Since ocean mesoscale features have time scales of weeks (Jacobs et al., 2001), it should be expected that errors are correlated in time. The experiments altering the increment insertion interval (B2), flow dependent covariance (B3, B4), and additional changes in

the data time window (B5, B7) do not significantly improve the results.

The experiment combining the new S_b with the emulation of long time correlation is B6, and this shows the best performance with the most occurrences of small velocity magnitude error (Fig. 14), more occurrences of low errors in direction than R1 though not as good as R2 (Fig. 15) and the best performance in terms of most occurrences of low errors in magnitude of velocity difference (Fig. 16). The use of a long time window forces the model solution to match the data within the time window. R5 suffers from the fact that the solution must match the average of the observations used in the analysis. As the observation time window increases, the analysis weakens horizontal gradients resulting in correspondingly weaker currents. Experiment B6 avoids this problem by applying the analysis increment over a long period with reduced amplitude that allows the dynamical system to maintain the horizontal gradients with increased current magnitudes.

Fig. 17 provides a summary spatial distribution of the RMS vector difference magnitudes in R1, that is $\sqrt{1/N \sum_i (u_{mi} - u_{oi})^2 + (v_{mi} - v_{oi})^2}$, where u_{mi} and u_{oi} are model and observed velocities respectively. These statistics are computed in $1/8^\circ$ bins, and only bins with more than 30 samples are shown. The data are separated for August and September. Areas of larger error are situated in the fronts of the mesoscale features, which move through August and September. The area along the northern

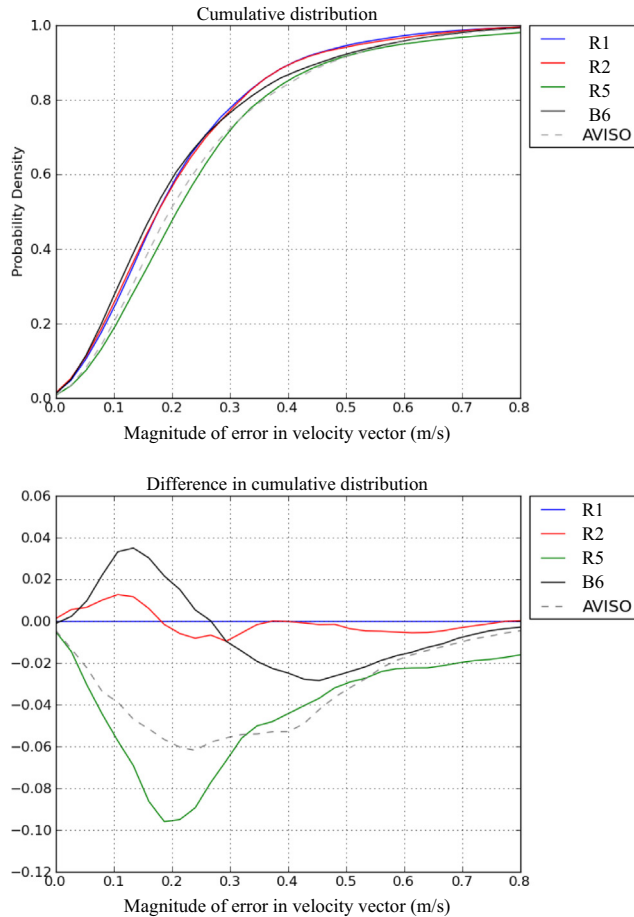


Fig. 16. (Top) cumulative distributions of the magnitude of velocity difference between the model experiments and the GLAD drifter inferred velocities. (Bottom) to better visualize the differences, the distribution of R1 is subtracted from all the experiments. The B6 experiment has the highest number of occurrences at low errors and therefore is performing best.

edge of the Loop Current Eddy has large errors associated with the First Cyclone (FC) advecting southeastward. The FC can be seen in the drifter tracks of Fig. 5 on August 15 at 27°N 88°W. The FC being less than 50 km across can be marginally resolved in the models, though it is smaller than what could be expected to be captured by the satellite observations. The boundaries of the AC on the Florida shelf are apparent as are the currents to the northwest between 87 and 88°W 27°N.

The spatially distributed errors of the perturbed covariance experiments are shown in Fig. 18, and the circulation features of Fig. 4 are superimposed. For a clearer comparison, the difference in the statistics for each experiment and those of R1 are shown for August and September. Blue areas show errors lower than R1, and red areas are errors higher than R1. Experiment R5 indicates the degradation in velocity performance in August with increased errors in the FC along the northern LCE edge, the bifurcation point at 85.5°W 27°N, the Florida shelf AC and an overall increase in errors in September in the northwestward flow. Experiments R2 and B6 both indicate substantial improvement over R1 and R5. During August, R2 predicts the FC along the LCE front with lower errors than B6. Relative to experiment R2 in August, B6 improves the bifurcation circulation at 85.5°W 27°W, the Florida shelf AC, and the SC circulation at 87°W 28°N. During September, B6 generally decreases overall error levels throughout the region relative to R2. Thus experiment B6 indicates improved performance across more mesoscale features than the other experiments.

5.3. Interpretation in the context of 4DVar

A 4DVar assimilation can be reduced through simplifying assumptions to produce the 3DVar used here. It is useful to examine the assumptions to provide insight to the aspects 3DVar is neglecting and how those assumptions are reflected in the results. Consider the 4DVar solution that minimizes errors relative to a time-evolving background state \mathbf{x}_b , observations \mathbf{y} and the dynamics \mathbf{A} , i.e., that minimizes the cost function J :

$$J = \frac{1}{2} \delta\mathbf{x}^T \mathbf{P}_b^{-1} \delta\mathbf{x} + \frac{1}{2} \delta\mathbf{x}^T \mathbf{A}^T \mathbf{W}^{-1} \mathbf{A} \delta\mathbf{x} + \frac{1}{2} (\mathbf{H} \delta\mathbf{x} - \mathbf{d})^T \mathbf{R}^{-1} (\mathbf{H} \delta\mathbf{x} - \mathbf{d}) \quad (5)$$

where $\delta\mathbf{x}$ is the analysis increment, \mathbf{P}_b is the background error covariance, \mathbf{A} is the tangent linearization of the dynamical system around the background state, \mathbf{W} is the dynamical error covariance, \mathbf{H} is the linearized observation operator, $\mathbf{d} = (\mathbf{y} - \mathbf{H}(\mathbf{x}_b))$ is the misfit of the observations to the background state \mathbf{x}_b and \mathbf{R} is the observation error covariance. A particular choice of covariances in the 4DVar can reduce it to the 3DVar. Consider the 4DVar applied over the entire time period of interest (60 days). All model variables at all locations and over all time steps are concatenated to form a single vector representing the model state trajectory \mathbf{x}_b through the entire time period. Assume that the temporal structure of background error covariance \mathbf{P}_b is taken to be a sum of Dirac delta functions at the analysis times of the 3DVar $\delta(t - t_{ai})$, where t_{ai} is the time of the i th 3DVar analysis. This results in \mathbf{P}_b being block diagonal with blocks providing the interrelations amongst variables only at each analysis time. Assume that observations occur only at the analysis times. The solution to (5) can be obtained by an inversion conducted at each successive analysis time. Assume the solution is a strong constraint except at the analysis times, and thus satisfies the dynamics. Once the i th inversion is conducted, the time-evolving state is computed simply by integrating the analysis forward to the next analysis time. Under these conditions, (5) represents the cost function for a cycling 3DVar.

The block diagonal form of \mathbf{P}_b carries strong implications. Background errors beyond the analysis time are assumed to be uncorrelated. This is convenient for solving the problem in that the analysis can be computed for each cycle independently. However, this formulation precludes consideration of errors correlated beyond one assimilation cycle. Fig. 10 shows that error correlations extend out to days. Thus, when considered from the 4DVar perspective, the cycling interval defined in a 3DVar imposes an assumption limiting the background error time correlation.

A 4DVar system can use a long time window in the analysis, and its contribution to reducing the analysis error covariance is computed theoretically for linear systems by Lewis et al. (2006). The authors also provide a detailed derivation of the difference between the analysis error covariances of the 4DVar and the Kalman filter (of which 3DVar is a special case), which includes a proof that the Kalman filter solution error covariance is always greater than or equal to the 4DVar solution error covariance. The difference lies in the 4DVar ability to propagate the observation information further in space and time. The implicit restriction imposed by the 3DVar assimilation cycle results in an increase in error levels.

The improved formulation for the variance amplitude \mathbf{S}_b demonstrated here can also be used in the 4DVar. However, as discussed above, error levels in the 3DVar are expected to be higher than the 4DVar. While a similar algorithm for estimating the background error variance may be used with a 4DVar, the amplitudes must be smaller.

For global daily predictions that are computationally intensive, a 4DVar solution is not feasible. Thus there is continued need to understand both the 3DVar and 4DVar approaches. Analytic formulations do not represent many complex relations within \mathbf{P}_b , thus Fu (2012) estimates \mathbf{P}_b based on historical model runs for methods such as ensemble optimal interpolation (EnOI) and shows benefits

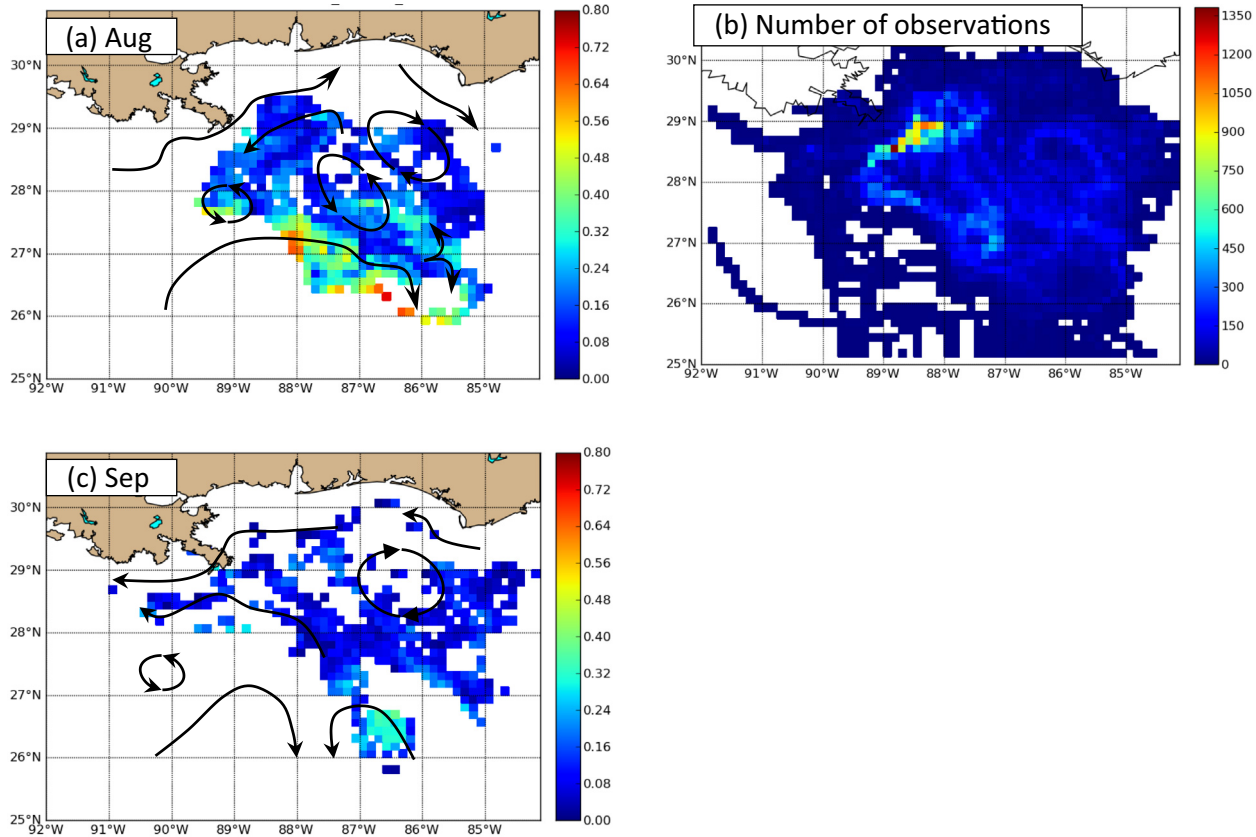


Fig. 17. (b) Number of observations in $1/8^\circ$ bins during August and September 2012 and RMS magnitude of the vector velocity error of experiment R1 during August (a) and September (c). Errors are shown only in bins with more than 30 observations. Error colorbars are in m/s.

over 3DVar. However, basing \mathbf{P}_b entirely on model covariances can introduce errors due to biases and drifts in the models. A stationary \mathbf{P}_b as implemented by Oke et al. (2010) avoids problems in model drifts, but it may still be influenced by biases. This motivates the hybrid approach in which \mathbf{P}_b is specified as a linear combination of model covariances and covariances based on functional formulations as in Eq. (2) (Gao et al., 2013).

Another perspective on the time correlation comes from the Rapid Environmental Assessments in which a large-scale survey provides an initial state. Attempting to correct a system based on under sampled features results in poor performance. On a daily basis, the satellite coverage is unable to resolve mesoscale features as can be seen in Fig. 10, which shows days with very little satellite data. Thus it is not possible to accurately correct these features using only daily data. Data spanning several days can begin to resolve features. However, a negative consequence is that a 3DVar analysis results in a state averaged over the data time window. In addition, using the observations multiple times without correcting the observation error level over-constrains the solution to the observations. These are the problems causing poor performance in R5. The temporal averaging results in weak horizontal gradients and thus weak currents. The R5 distribution of error in magnitude (Fig. 14) and distribution of magnitude of velocity difference (Fig. 16) suffer due to this problem. The R5 distribution of direction errors (Fig. 15) does not suffer as badly. There are roughly equal occurrences of direction errors less than 35 degrees as for R1. Experiment B6 mitigates the deficiencies in using observations multiple times by emulating the effect of a long time correlation through dividing the analysis increment by the number of days in the increment insertion interval. As shown in Fig. 11, the increments in B6 are very small and applied over many days.

The results from B6 indicate much improved performance over R5 in the distribution of difference in magnitude and magnitude of the velocity differences. B6 has the highest fraction of occurrences at the low error levels of all the experiments (including those not shown). The directional errors in B6 show advancement over R1 at low values but are somewhat degraded relative to R2.

6. Discussion

The GLAD experiment shows it is now possible to begin testing underlying assumptions of ocean assimilation methods, which has not been extensively possible before. While persistently sampling several mesoscale features at high resolution over two months, the data set is still just one experiment and exists only in the Gulf of Mexico. The results and conclusions should be transferable to other regions and to global mesoscale prediction as well. However, predictive skill varies within different dynamical regions such as the Gulf Stream and Kuroshio currents vs. the South China Sea (Metzger et al., 2014b). Because the Gulf of Mexico is enclosed, prediction skill is higher in this basin using the same metrics (Metzger et al., 2014a). Also, mesoscale prediction skill is highly dependent on the quantity and coverage of altimeter observations (Ananda et al., 2006; Smedstad et al., 2003; Jacobs et al., 2014).

The GLAD data point to additional underlying considerations in future direction of ocean assimilation. Many ocean data assimilation methods are formulated with the objective to predict the ocean mesoscale as developed through the GODAE program (Cummings et al., 2009). This objective is feasible given the altimeter observations, which, though sparse in space and time, are capable of sampling a portion of the mesoscale wavenumber and

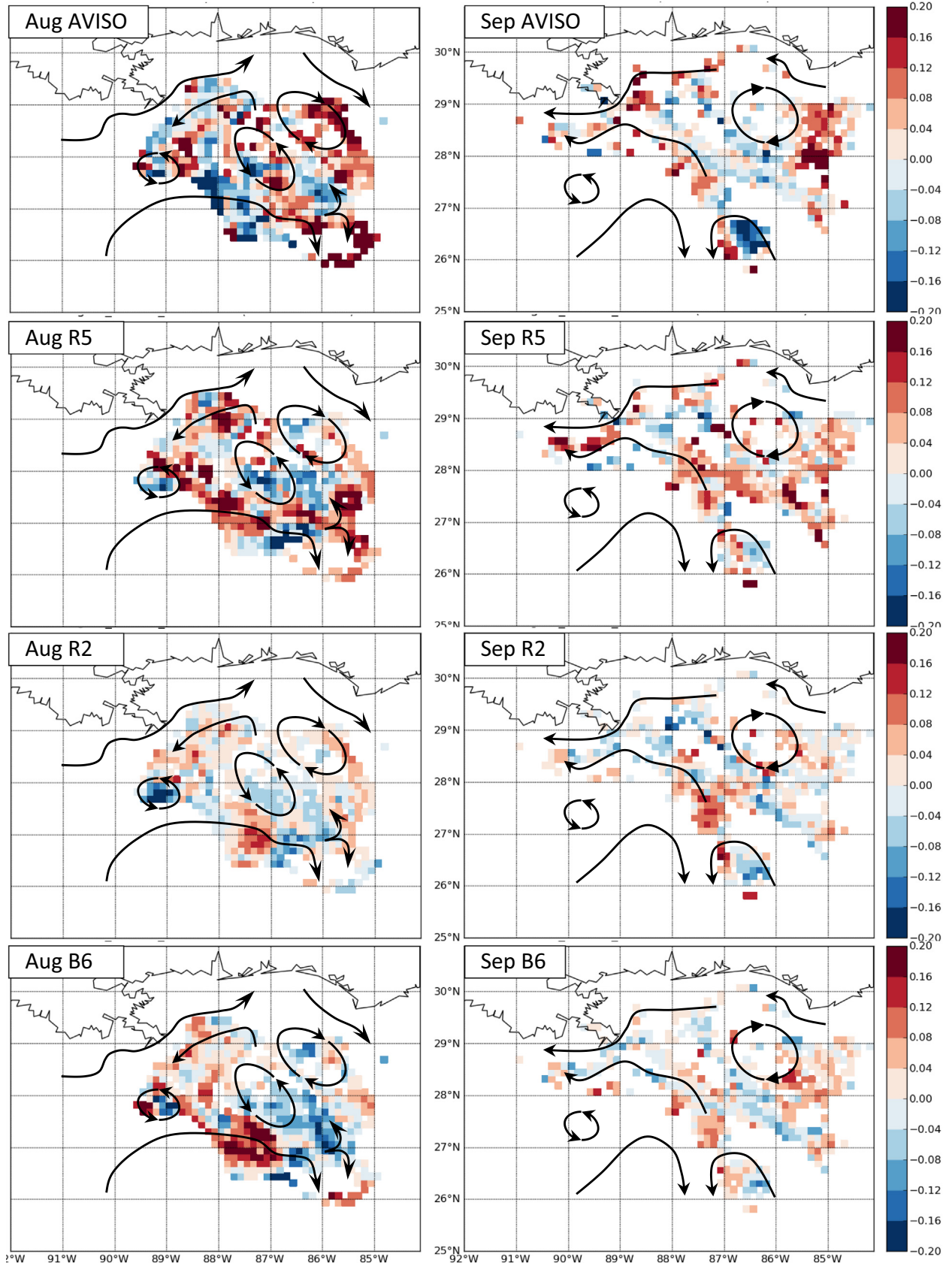


Fig. 18. Differences between RMS magnitudes of the vector velocity error computed for R1 and other experiments. Error levels of square root of mean of vector error magnitude squared differenced from experiment R01. Only bins with more than 30 observations are shown. August and September 2012 are shown separately. The circulation features of Fig. 4 are superimposed. Colorbar units are in m/s.

frequency spectrum (Traon and Dibarbour, 1999). The long time scales of the ocean result in a mesoscale feature being sampled several times over a decorrelation time of one month or more. One area that cannot yet be constrained with in assimilation is the submesoscale which is not resolved by the altimeter observations, has large Rossby number and high ageostrophic currents (Capet et al., 2008; Mensa et al., 2013; Zhong and Bracco, 2013).

Three fundamental capabilities must exist to address the submesoscale. The first is observations. GLAD is a demonstration that sufficient coverage and persistence of observations at scales below the mesoscale are achievable. Other planned observation systems include the Surface Water/Ocean Topography (SWOT) satellite mission planned to provide full global 2D sea surface height imaging with a resolution of kilometers (Durand et al., 2010; Fu and Ferrari, 2008).

The second capability lies in multiscale data assimilation. Basic research has yielded algorithms that solve the assimilation problem sequentially over scales (Brandt and Zaslavsky, 1997; Choi et al., 2008; Haley and Lermusiaux, 2010; Lermusiaux, 2002). Application to the submesoscale requires a first multiscale iteration assimilating the mesoscale information. This problem has been well studied. The second multiscale iteration should then address the submesoscale.

The third capability must provide a new \mathbf{P}_b for the submesoscale that removes assumptions present in \mathbf{P}_b for the mesoscale iteration. Amongst these are geostrophic balance relations between the mass and velocity fields that are inappropriate for the submesoscale as well as vertical relations in the water column. Solving the submesoscale iteration of multiscale assimilation requires revisiting the background error covariance \mathbf{P}_b that will have distinctly different horizontal, vertical and temporal structures than the mesoscale. Once again, we will be required to test new \mathbf{P}_b formulations for the submesoscale.

7. Conclusions

Our analysis shows that background error variance amplitude and time correlation are the most sensitive components within the background error covariance \mathbf{P}_b . The extraordinarily dense GLAD data set provides substantially greater information to investigate the relative importance of assumptions in the components of \mathbf{P}_b . This is a problem not previously addressable due to sparse observations. The assimilation systems are used to emulate the long time correlations by using data over several prior days in each daily cycle. When using data multiple times, the modeled currents are weak due to the analysis providing a best estimate to match an average over 7 days. This is alleviated by dividing the analysis increment fields by the data time window length to more properly weight the data. The results pave the way toward implementations that can properly account for the time correlations important in 3DVar and are more explicitly apparent and controllable in 4DVar through the analysis time window. While 4DVar can take into account a longer influence time of observations, care must be taken to ensure the analysis window is sufficiently long to account for the long time correlation in the ocean.

A study such as this would not be possible without an extensive set of observations covering a significant number of mesoscale features for a sustained time period. Prior hypothesized formulations for the background error variance amplitude and time correlation are rejected in favor of new understanding. Such data sets become reference points that are used throughout future research. The GLAD experiment points the direction toward the future.

Acknowledgments

This research is funded by a Grant from BP/The Gulf of Mexico Research Initiative to the Consortium for Advanced Research on the Transport of Hydrocarbon in the Environment (CARTHE). The GLAD drifter trajectory dataset used here is publicly available (<http://dx.doi.org/10.7266/N7VD6WC8>). This paper is contribution NRL/JA/7320–11-1001 and has been approved for public release.

References

- Ananda, P., Yannice, F., Gilles, L., Le Traon, P.-Y., 2006. Improved description of the ocean mesoscale variability by combining four satellite altimeters. *Geophys. Res. Lett.* 33, 13–16.
- Barron, C.N., Kara, A.B., Hurlburt, H.E., Rowley, C., Smedstad, L.F., 2004. Sea surface height predictions from the global navy coastal ocean model (NCOM) during 1998–2001. *J. Atmos. Oceanic Technol.* 21 (12), 1876–1893.
- Barron, C.N., Kara, A.B., Martin, P.J., Rhodes, R.C., 2006. Formulation, implementation and examination of the vertical coordinate choices in the global Navy coastal ocean model (NCOM). *Ocean Modell.* 11 (3), 347–375.
- Barron, C.N., Kara, A.B., Rhodes, R.C., Rowley, C., Smedstad, L.F., 2007. Validation Test Report for the 1/8 Global Navy Coastal Ocean Model Nowcast/Forecast System, NRL Tech Report NRL/MR/7320-07-9019.
- Bell, M.J., Lefebvre, M., Le Traon, P.Y., Smith, N., Wilmer-Becker, K., 2009. GODAE The global ocean data assimilation experiment. *Oceanography* 22 (3), 14–21.
- Bennett, A.F., 2002. Inverse modeling of the ocean and atmosphere, Cambridge, ISBN 0-521-81373-5, 235 pp.
- Brandt, A., Zaslavsky, L.Y., 1997. Multiscale algorithm for atmospheric data assimilation. *SIAM J. Sci. Comput.* 18 (3), 949–956.
- Brasseur, P. et al., 2005. Data assimilation for marine monitoring and prediction: the MERCATOR operational assimilation systems and the MERSEA developments. *Q. J. R. Meteor. Soc.* 131 (613), 3561–3582.
- Capet, X., McWilliams, J.C., Mokemaker, M.J., Shchepetkin, A.F., 2008. Mesoscale to submesoscale transition in the California current system. Part I: flow structure, eddy flux, and observational tests. *J. Phys. Oceanogr.* 38 (1), 29–43.
- Carnes, M.R., Helber, R.W., Barron, C.N., Dastugue, J.M., 2010. Validation Test Report for GDEM4, NRL Report NRL/MR/7330-10-9271.
- Carrier, M.J., Ngodock, H., 2010. Background-error correlation model based on the implicit solution of a diffusion equation. *Ocean Modell.* 35 (1–2), 45–53.
- Choi, H., McDowell, D.L., Allen, J.K., Rosen, D., Mistree, F., 2008. An inductive design exploration method for robust multiscale materials design. *J. Mech. Des.* 130 (3).
- Cobas-Garcia, M., Gomez-Tato, A., Cotelo-Queijo, C., Vazquez-Cendon, M.E., Carracedo-Garcia, P., Costa, P., Ruiz-Villarreal, M., 2012. First approach to the application of operational 4DVAR data assimilation to the regional ocean model system. *Numer. Methods Hyperbolic Equ.*, 393.
- Coelho, E.F., Hogan, P., Jacobs, G., Thoppil, P., Huntley, H., Haus, B., Lipphardt, B., Jr., Kirwan, A.D., Jr., Ryan, E., Olascoaga, J., Novelli, G., Beron-Vera, F., Haza, A., Poje, A., Griffa, A., Ozgokmen, T., Bogucki, D., Chen, S., Curcic, M., Iskandarani, M., Judt, F., Laxague, N., Mariano, A., Reniers, A., Smith, C., Valle-Levinson, A., Wei, M., 2014. Ocean current estimation using a multi-model ensemble Kalman filter during the grand lagrangian deployment experiment (GLAD), Ocean Modeling, Virtual Special Issue (VSI): gulf of Mexico modelling: lessons learned from the spill (in review OCEDM D-13-00166).
- Crosby, D.S., Breaker, L.C., Gemmill, W.H., 1993. A proposed definition for vector correlation in geophysics: theory and application. *J. Atmos. Oceanic Technol.* 10, 355–357.
- Cummings, J.A., Smedstad, O.M., 2013. Variational data assimilation for the global ocean data assimilation for atmospheric. *Oceanic Hydrol. Appl. II*, Chapter 13.
- Cummings, J., Bertino, L., Brasseur, P., Fukumori, I., Kamachi, M., Martin, M.J., Mogensen, K., Oke, P., Testut, C.E., Verron, J., Weaver, A., 2009. Ocean data assimilation systems for GODAE. *Oceanography* 22 (3), 96–109. <http://dx.doi.org/10.5670/oceanog.2009.69>.
- Cummings, J.A., 2005. Operational multivariate ocean data assimilation. *Q. J. Roy. Meteor. Soc.* 131 (613), 3583–3604.
- Daley, R., 1996. *Atmospheric Data Analysis*. Cambridge University Press, 438 pp.
- Daley, Roger R., Barker, Edward E., 2001. NAVDAS Source Book: NRL Atmospheric Variational Data Assimilation System. NRL Publication NRL/PU/7530-01-441, Monterey, CA, 160 pp.
- Davis, R.E., 1985. Drifter observations of coastal surface currents during CODE: the method and descriptive view. *J. Geophys. Res.* 90, 4741–4755.
- Derber, John, Rosati, Anthony, 1989. A global oceanic data assimilation system. *J. Phys. Oceanogr.* 19, 1333–1347, [http://dx.doi.org/10.1175/1520-0485\(1989\)019<1333:AGODAS>2.0.CO;2](http://dx.doi.org/10.1175/1520-0485(1989)019<1333:AGODAS>2.0.CO;2).
- Durand, M., Lee-Lueng, F., Lettenmaier, D.P., Alsdorf, D.E., Rodriguez, E., Esteban-Fernandez, D., 2010. The surface water and ocean topography mission: observing terrestrial surface water and oceanic submesoscale Eddies. *Proc. IEEE* 98 (5), 766–779. <http://dx.doi.org/10.1109/JPROC.2010.2043031>.
- Fox, D.N., Barron, C.N., Carnes, M.R., Boada, M., Peggion, G., Gurley, J.V., 2002. The modular ocean data assimilation system. *Oceanography* 15 (1), 22–28. <http://dx.doi.org/10.5670/oceanog.2002.33>.
- Fu, Lee-Lueng, 2010. Determining ocean circulation and sea level from satellite altimetry: progress and challenges. *Oceanogr. Space.* 147–163.

- Fu, W.W., 2012. Altimetric data assimilation by EnOI and 3DVAR in a tropical pacific model: impact on the simulation of variability. *Adv. Atmos. Sci.* 29 (4), 823–837.
- Fu, L.-L., Ferrari, R., 2008. Observing oceanic submesoscale processes from space. *Eos Trans. Am. Geophys. Union* 89 (48). <http://dx.doi.org/10.1029/2008EO480003>, 488–488.
- Gao, J.D., Xue, M., Stensrud, D.J., 2013. The development of a hybrid EnKF-3DVAR algorithm for storm-scale data assimilation. *Adv. Meteorol.*
- Gaspari, G., Cohn, S.E., 1999. Construction of correlation functions in two and three dimensions. *Q. J. R. Meteorol. Soc.* 125, 723–757.
- Gawarkiewicz, G. et al., 2011. Circulation and intrusions northeast of Taiwan: chasing and predicting uncertainty in the cold dome. *Oceanography* 24 (4), 110–121.
- Haley, P.J., Lermusiaux, P.F.J., 2010. Multiscale two-way embedding schemes for free-surface primitive equations in the "Multidisciplinary Simulation, Estimation and Assimilation System". *Ocean Dyn.* 60 (6), 1497–1537.
- Haller, G., Beron-Vera, F.J., 2012. Geodesic theory of transport barriers in two-dimensional flows. *Physica D* 241 (20), 1680–1702.
- Haller, G., Yuan, G., 2000. Lagrangian coherent structures and mixing in two-dimensional turbulence. *Physica D* 147, 352–370.
- Hodur, R.M., 1997. The naval research laboratory's coupled ocean/atmosphere mesoscale prediction system (COAMPS). *Mon. Weather Rev.* 125, 1414–1430. <http://dx.doi.org/10.1175/1520-0493>.
- Jacobs, G.A., Barron, C.N., Rhodes, R.C., 2001. Mesoscale characteristics. *J. Geophys. Res.* 106 (C9), 19581–19595.
- Jacobs, G.A., Richman, J.G., Doyle, J.D., Spence, P.L., Bartels, B.P., Barron, C.N., Helber, R.W., Bub, F.L., 2014. Simulating conditional deterministic predictability within ocean frontogenesis. *Ocean Modell.* 78, 1–16.
- Janeković, I., Powell, B.S., Matthews, D., McManus, M.A., Sevadjian, J., 2013. 4D-Var data assimilation in a nested, coastal ocean model: a Hawaiian case study. *J. Geophys. Res. Oceans* 118 (10), 5022–5035.
- Kalnay, E., 2003. Atmospheric modeling, data assimilation, and predictability. Cambridge university press.
- Le Traon, P.Y., Dibarbour, G., 2002. Velocity mapping capabilities of present and future altimeter missions: the role of high-frequency signals. *J. Atmos. Oceanic Technol.* 19, 2077–2087. [http://dx.doi.org/10.1175/1520-0426\(2002\)019](http://dx.doi.org/10.1175/1520-0426(2002)019).
- Lermusiaux, P.F.J., 2002. On the mapping of multivariate geophysical fields: sensitivities to size, scales, and dynamics. *J. Atmos. Oceanic Technol.* 19 (10), 1602–1637.
- Leslie, W., Robinson, A.R., Haley, P., Logotou, O., Lermusiaux, P., Coelho, E.F., 2008. Verification and training of real-time forecasting of multi-scale ocean dynamics for MREA. *J. Mar. Syst.* 69 (1–2), 3–16.
- Lewis, J.M., Lakshmivarahan, S., Dhall, S., 2006. Dynamic Data Assimilation: A Least Squares Approach. Cambridge University Press, ISBN 9780521851558, 680 pp.
- Lozano, C.J., Robinson, A.R., Arango, H.G., Gangopadhyay, A., Sloan, N.Q., Haley, P.J., Leslie, W.G., 1996. An interdisciplinary ocean prediction system: assimilation strategies and structured data models.
- Malanotte-Rizzoli, P. (Ed.), 1996. Modern Approaches to Data Assimilation in Ocean Modelling. Elsevier Oceanography Series, vol. 61. Elsevier Science, pp. 413–452.
- Martin, A.J., Hines, A., Bell, M.J., 2007. Data assimilation in the FOAM operational short-range ocean forecasting system: a description of the scheme and its impact. *Q. J. R. Meteorol. Soc.* 133 (625), 981–995.
- Martin, P.J., Barron, C.N., Smedstad, L.F., Campbell, T.J., Wallcraft, A.J., Rhodes, R.C., Rowley, C., Townsend, T.L., Carroll, S.N., 2009. User's Manual for the Navy Coastal Ocean Model (NCOM) version 4.0, NRL Report NRL/MR/7320-09-9151.
- Mensa, J.A., Garraffo, Z., Griffa, A., Özgökmen, T.M., Haza, A., Veneziani, M., 2013. Seasonality of the submesoscale dynamics in the Gulf Stream region. *Ocean Dyn.* 63 (8), 923–941. <http://dx.doi.org/10.1007/s10236-013-0633-1>.
- Metzger, E.J., Hurlbert, H.E., Wallcraft, A.J., Shriner, J.F., Townsend, T.L., Smedstad, O.M., Thoppil, P.G., Franklin, D.S., Peggion, G., 2010. Validation Test Report for the Global Ocean Forecast System V3.0 – 1/12° HYCOM/NCODA: Phase II, NRL Reports NRL/MR/7320-10-9236.
- Metzger, E.J., 2014. Predictability on the Gulf of Mexico from the global 1/12° HYCOM system, unpublished results.
- Metzger, E.J., Smedstad, O.M., Thoppil, P.G., Hurlbert, H.E., Cummings, J.A., Wallcraft, A.J., DeHaan, C.J., 2014b. US Navy operational global ocean and Arctic ice prediction systems. *Oceanography* 27 (3), 32–43.
- Ngodock, H., Carrier, M., 2014. A 4D-Var system for the Navy coastal ocean model Part I: system description and assimilation of synthetic observations in the Monterey Bay. *Mon. Weather Rev.*
- Ohlmann, J.C., Niiler, P.P., Fox, C.A., Leben, R.R., 2001. Eddy energy and shelf interactions in the Gulf of Mexico. *J. Geophys. Res.* 106, 2605–2620.
- Oke, P.R., Brassington, G.B., Griffin, D.A., Schiller, A., 2008. The Bluelink ocean data assimilation system (BODAS). *Ocean Modell.* 21 (1–2), 46–70. <http://dx.doi.org/10.1016/j.ocemod.2007.11.002>.
- Oke, P.R., Brassington, G.B., Griffin, D.A., Schiller, A., 2010. Ocean data assimilation: a case for ensemble optimal interpolation. *Aust. Meteorol. Oceanogr.* 59, 67–76.
- Olascoaga, M.J., Beron-Vera, F.J., Haller, G., Trinanes, J., Iskandarani, M., Coelho, E.F., Haus, B., Huntley, H.S., Jacobs, G., Kirwan Jr., A.D., Lippard Jr., B.L., Ozgokmen, T., Reniers, A.J.H.M., 2013. Drifter motion in the Gulf of Mexico constrained by altimetric Lagrangian coherent structures. *Geophys. Res. Lett.* 40, 6171–6175. <http://dx.doi.org/10.1002/2013GL058624>.
- Pascual, A., Faugère, Y., Larnicol, G., Le Traon, P.-Y., 2006. Improved description of the ocean mesoscale variability by combining four satellite altimeters. *Geophys. Res. Lett.* 33, L02611. <http://dx.doi.org/10.1029/2005GL024633>.
- Poje, Andrew C., Özgökmen, Tamay M., Lippard Jr, Bruce, Lippard Jr, Bruce, Haus, Brian K., Ryan, Edward H., Haza, Angelique C., Reniers, A.J.H.M., Olascoaga, Josefina, Novelli, Guillaume, Beron-Vera, Francisco J., Chen, Shuyi, Mariano, Arthur J., Jacobs, Gregg, Hogan, Pat, Coelho, Emanuel, Kirwan Jr, A.D., Huntley, Helga, Griffa, Annalisa, 2014. Submesoscale dispersion in the vicinity of the Deepwater Horizon spill. *Proc. Nat. Acad. Sci.* 111 (35), 12693–12698.
- Robinson, A.R., 1997. Forecasting and simulating coastal ocean processes and variabilities with the harvard ocean prediction system (HOPS). In: Pouliquen, E., Kirwan, A.D., Jr., Pearson, R.T. (Eds.). SACLANTCEN Conference Proceedings Series CP-44, ISBN 88-900194-0-9.
- Rowley, C., 2010. Validation Test Report for the RELO System, Oceanography Division, Naval Research Laboratory, Stennis Space Center, MS, NRL Report, NRL/MR/7320-10-9216, 69 pp.
- Rowley, C., Martin, P.J., Cummings, J.A., 2010. The naval research laboratory relocatable ocean nowcast/forecast system. *US Navy J. Underwater Acoust.* 60 (1), 169–202.
- Saha, S. et al., 2010. The NCEP climate forecast system reanalysis. *Bull. Am. Meteorol. Soc.* 91 (8), 1015–1057.
- Smedstad, O.M., Hurlbert, H.E., Metzger, E.J., Rhodes, R.C., Shriner, J.F., Wallcraft, A.J., Kara, A.B., 2003. An operational Eddy resolving 1/16 degrees global ocean nowcast/forecast system. *J. Mar. Syst.* 40, 341–361.
- Smith, S., Cummings, J.A., Rowley, C., Chu, P., Shriner, J., Helber, R., 2011. Validation Test Report for the Navy Coupled Ocean Data Assimilation 3D Variational Analysis (NCODA-VAR) System, Version 3.43, NRL Report NRL/MR/7320-11-9363.
- Talagrand, O., 2003. A posteriori validation of assimilation algorithms, in: Data assimilation for the earth system, edited, Springer, pp. 85–95.
- Traon, P.Y.L., Dibarbour, G., 1999. Mesoscale mapping capabilities of multiple-satellite altimeter missions. *J. Atmos. Oceanic Technol.* 16 (9), 1208–1223. [http://dx.doi.org/10.1175/1520-0426\(1999\)016<1208:MMCOMS>2.0.CO;2](http://dx.doi.org/10.1175/1520-0426(1999)016<1208:MMCOMS>2.0.CO;2).
- Weaver, A.T., Mirouze, I., 2013. On the diffusion equation and its application to isotropic and anisotropic correlation modelling in variational assimilation. *Q. J. R. Meteorol. Soc.* 139 (670), 242–260.
- Zhong, Y.S., Bracco, A., 2013. Submesoscale impacts on horizontal and vertical transport in the Gulf of Mexico. *J. Geophys. Res. Oceans* 118 (10), 5651–5668.